Electronic Supplementary Material (ESI) for Journal of Materials Chemistry C.

Supporting Information

The Effect of Inert Dopant Ions on Spin-Crossover Materials is not Simply Controlled by Chemical Pressure

Prabir Ghosh,[a] Christopher M. Pask,[b] Hari Babu Vasili,[c] Nobuto Yoshinari,[d] Takumi Konno,[d,e] Oscar Cespedes,[c] Cristian Enachescu,[f] Pradip Chakraborty*[g] and Malcolm A. Halcrow*[b]

[a]*Department of Mechanical Engineering, Indian Institute of Technology Kharagpur, Kharagpur-721302, India.*

[b]*School of Chemistry, University of Leeds, Woodhouse Lane, Leeds, UK LS2 9JT. E-mail: m.a.halcrow@leeds.ac.uk.*

[c]*School of Physics and Astronomy, W. H. Bragg Building, University of Leeds, Leeds, UK LS2 9JT.*

[d]*Department of Chemistry, Graduate School of Science, Osaka University, Toyonaka, Osaka 560-0043, Japan.*

[e]*Current address: Department of Chemistry, Faculty of Science, National Taiwan Normal University, Taipei 11677, Taiwan.*

[f]*Faculty of Physics, Alexandru Ioan Cuza University, 700506 Iasi, Romania.*

[g]*Department of Chemistry, Indian Institute of Technology Kharagpur, Kharagpur-721302, India. E-mail: pradipc@chem.iitkgp.ac.in*

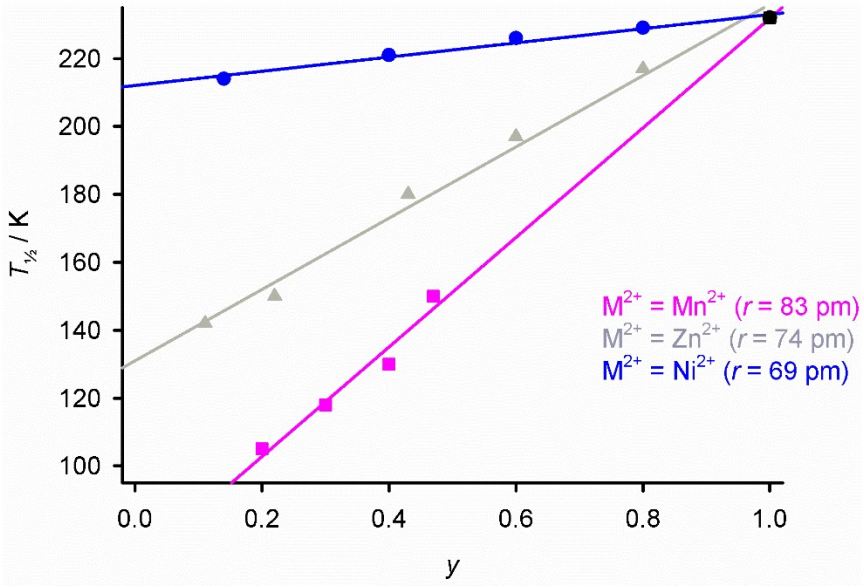

Figure S1 Variation of $T_{½}$ with composition in $[Fe_yM_{1-y}(3\text{-bpp})_2][NCSe]_2$ (3-bpp = 2,6-*bis*{1*H*-pyrazol-3-yl}pyridine, a regioisomer of the bpp ligand used in this work) with different dopant ions: M = Mn (■), Zn (▲) and Ni (●). The graph is replotted from ref. 1, and contains data from refs. 1-3. Trends are highlighted by linear regression lines generated from the data points for each dopant metal.

Errors on these values were not reported, but they should become larger at lower iron concentrations as *y* approaches zero.

All the dopant ions lower $T_{½}$, in the order: M = Mn > Zn > Ni. That is exactly the trend predicted from the ionic radii of the dopant ions (shown). Larger dopant ions lead to expansion of the lattice, thus reducing the chemical pressure about each iron centre. That stabilises the larger high-spin form of the iron complex (*r* = 78 pm) and reduces $T_{½}$, as observed.

Other families of doped SCO materials showing a similar metal ion dependence on $T_{½}$ include: $[Fe_yM_{1-y}(NCS)_2(btr)_2]\cdot H_2O$ (M = Zn, Co, Ni; btr = 4,4'-*bis*{1,2,4-triazole}),[4] $[Fe_yM_{1-y}(NCS)_2(phen)_2]$ (M = Cd, Mn, Zn, Co, Ni; phen = 1,10-phenanthroline),[5] $[Fe_yM_{1-y}(qnal)_2]$ (M = Zn, Ni; qnalH = *N*-{quinol-8-yl}-2-hydroxy-1-naphthaldimine)[6] and $[Fe_yM_{1-y}\{Pt(CN)_4\}(pyrazine)]$ (M = Co, Ni).[7]

By that logic, no isomorphous dopant should lead to an increase in $T_{½}$, since there is no common divalent ion with an ionic radius approaching that of low-spin Fe^{2+} (*r* = 61 pm). Hence, the stabilisation of the low-spin state by ruthenium doping in $[Fe_zRu_{1-z}(bpp)_2][BF_4]_2$ must have a different explanation.

Table S1 The metal content of the new $[Fe_zM_{1-z}(bpp)_2][BF_4]_2$ materials from EDX analysis.

	Element	Wt % First	Second	Third	Fourth	Fifth	Average
M = Zn							
1a	Fe	92.54	88.71	87.33	91.04	90.42	90 ± 2
	Zn	7.46	11.29	12.67	8.96	9.58	10 ± 3
1b	Fe	67.71	72.64	71.57	68.91	70.23	70 ± 2
	Zn	32.29	27.36	28.43	31.09	29.77	30 ± 2
1c	Fe	53.57	49.27	53.26	63.56	–	55 ± 5
	Zn	46.43	50.73	46.74	36.44	–	45 ± 5
1d	Fe	22.32	22.17	24.73	23.21	25.52	24 ± 2
	Zn	77.68	77.83	75.27	76.79	74.48	76 ± 2
1e	Fe	4.96	4.28	6.70	5.36	6.53	6 ± 1
	Zn	95.04	95.72	93.30	94.64	93.47	94 ± 1
M = Ru							
2a	Fe	89.42	85.26	82.29	81.02	–	84 ± 4
	Ru	10.58	14.74	17.71	18.98	–	16 ± 4
2b	Fe	62.41	59.96	64.89	63.87	72.51	65 ± 5
	Ru	37.59	40.04	35.11	36.13	27.49	35 ± 8
2c	Fe	49.45	52.78	45.28	51.53	48.78	50 ± 3
	Ru	50.55	47.22	54.72	48.47	51.22	50 ± 4
2d	Fe	9.15	17.79	16.90	13.24	12.67	14 ± 5
	Ru	90.85	82.21	83.10	86.76	87.33	86 ± 4

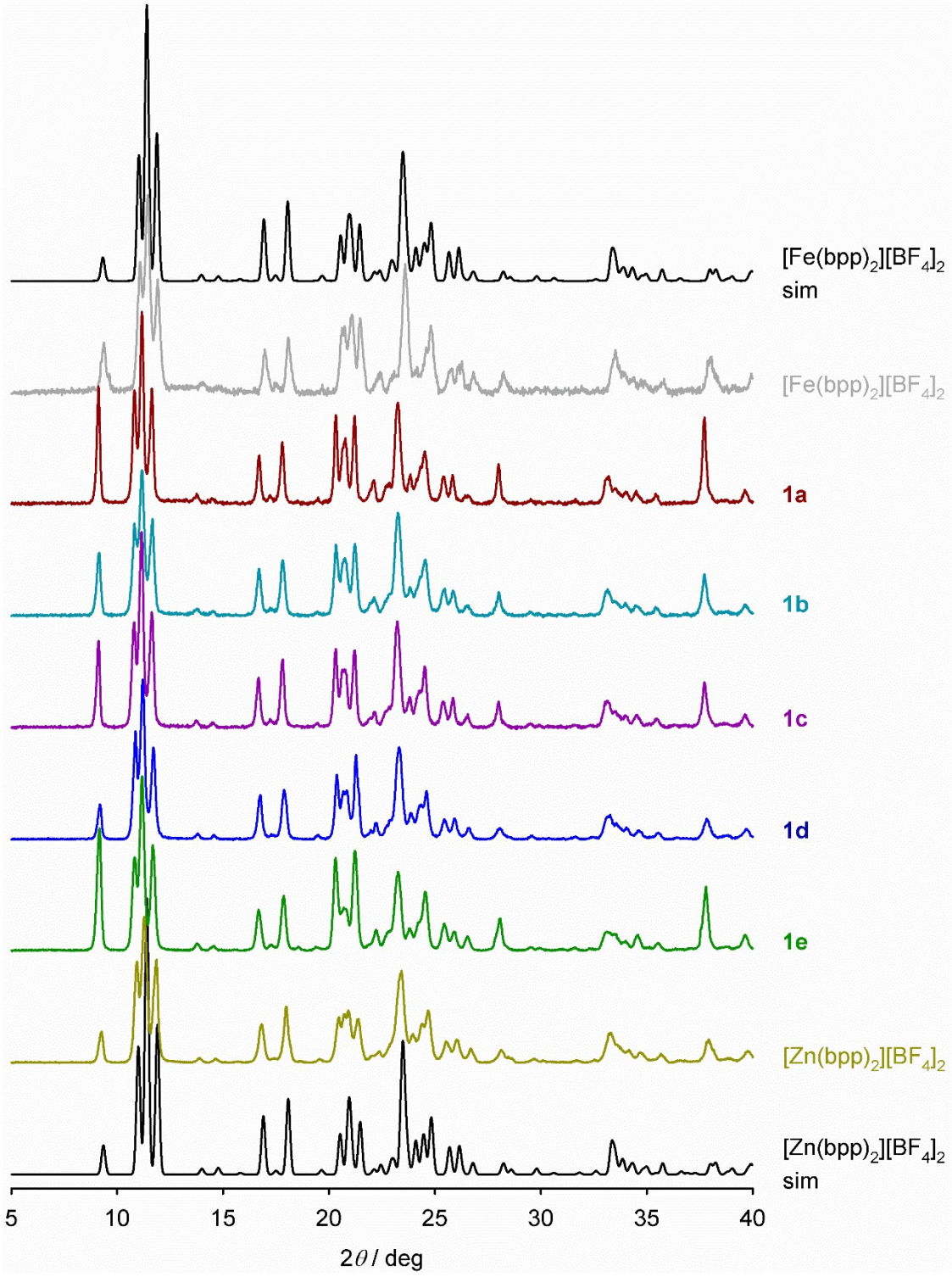

Figure S2 Room temperature X-ray powder diffraction data for **1a**-**1e**. Data from the pure iron and zinc precursor complexes, and simulations based on their published crystal structures,[8,9] are also included for comparison.

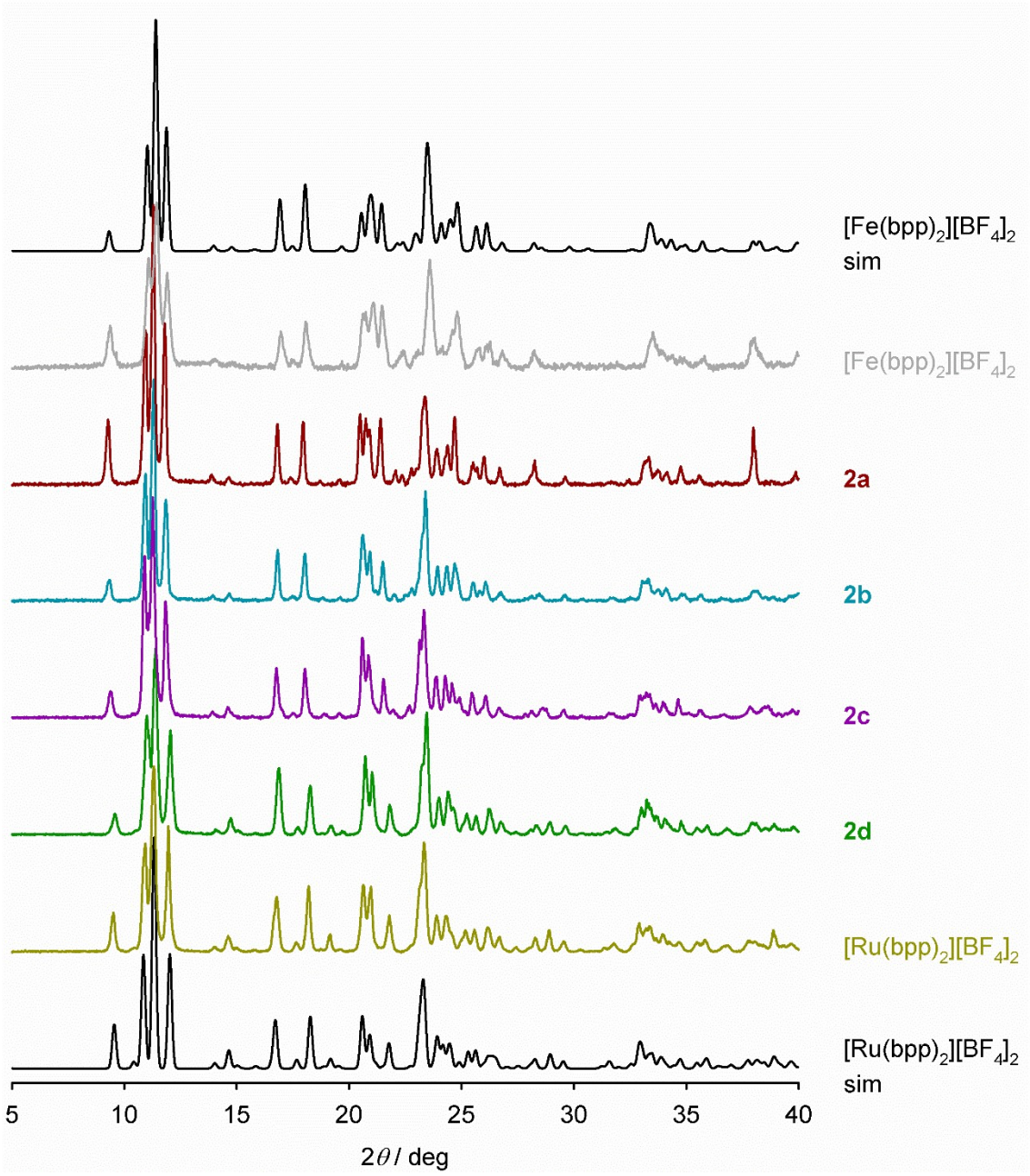

Figure S3 Room temperature X-ray powder diffraction data for **2a**-**2d**. Data from the pure iron and ruthenium precursor complexes, and simulations based on their published crystal structures,[8,10] are also included for comparison.

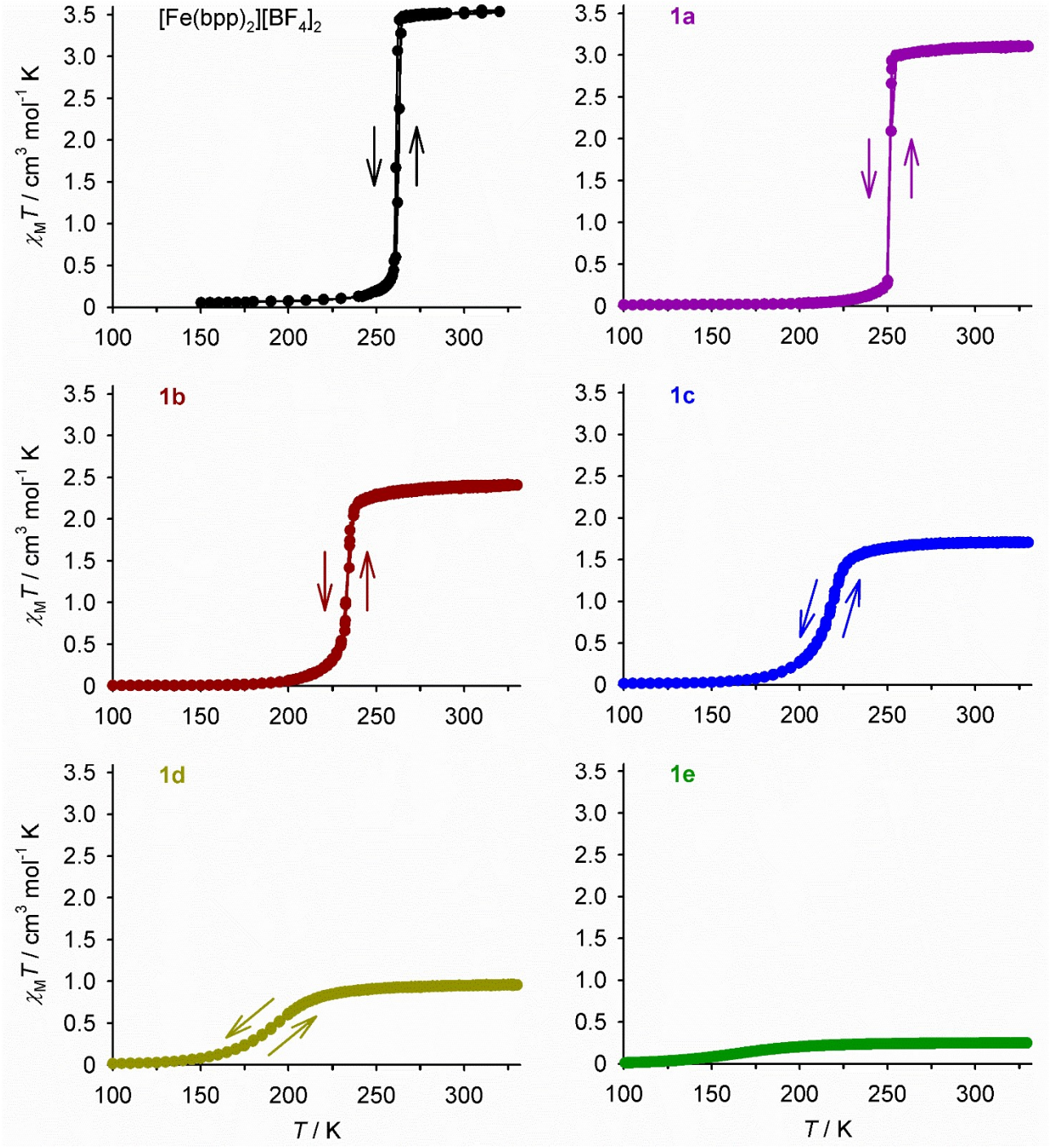

Figure S4 Variable temperature magnetic susceptibility data for $[Fe(bpp)_2][BF_4]_2$ and **1a-1e**. Data were collected at a scan rate of 2 K min^{-1} in cooling and warming modes, except for **1e** where only a cooling temperature ramp was employed. The data for $[Fe(bpp)_2][BF_4]_2$ are taken from ref. 11.

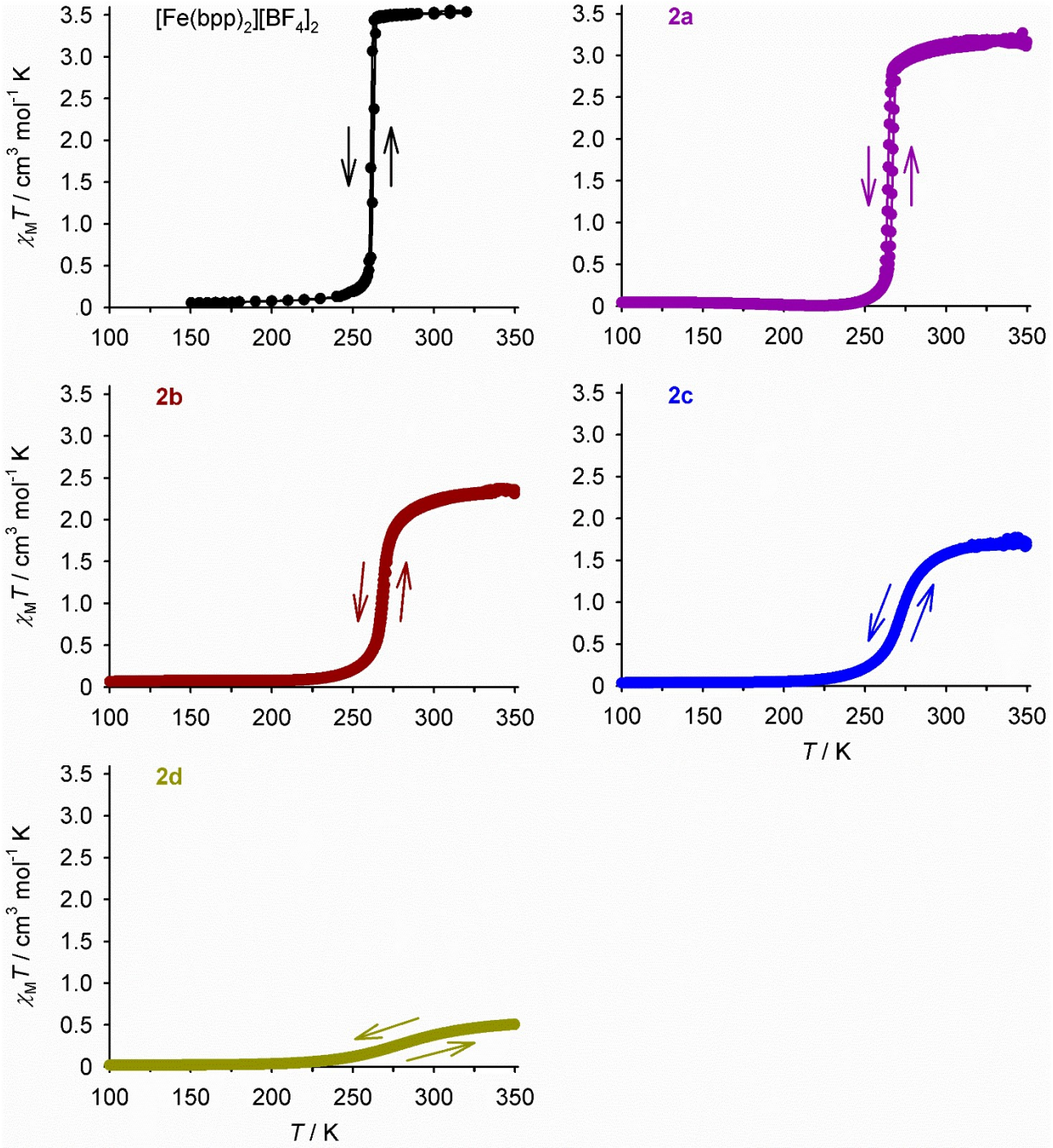

Figure S5 Variable temperature magnetic susceptibility data for $[Fe(bpp)_2][BF_4]_2$ and **2a-2d**. Data were collected in cooling and warming modes, at a scan rate of 2 K min^{-1}. The data for $[Fe(bpp)_2][BF_4]_2$ are taken from ref. 11.

The temperature scale in this graph is different from Figure S4.

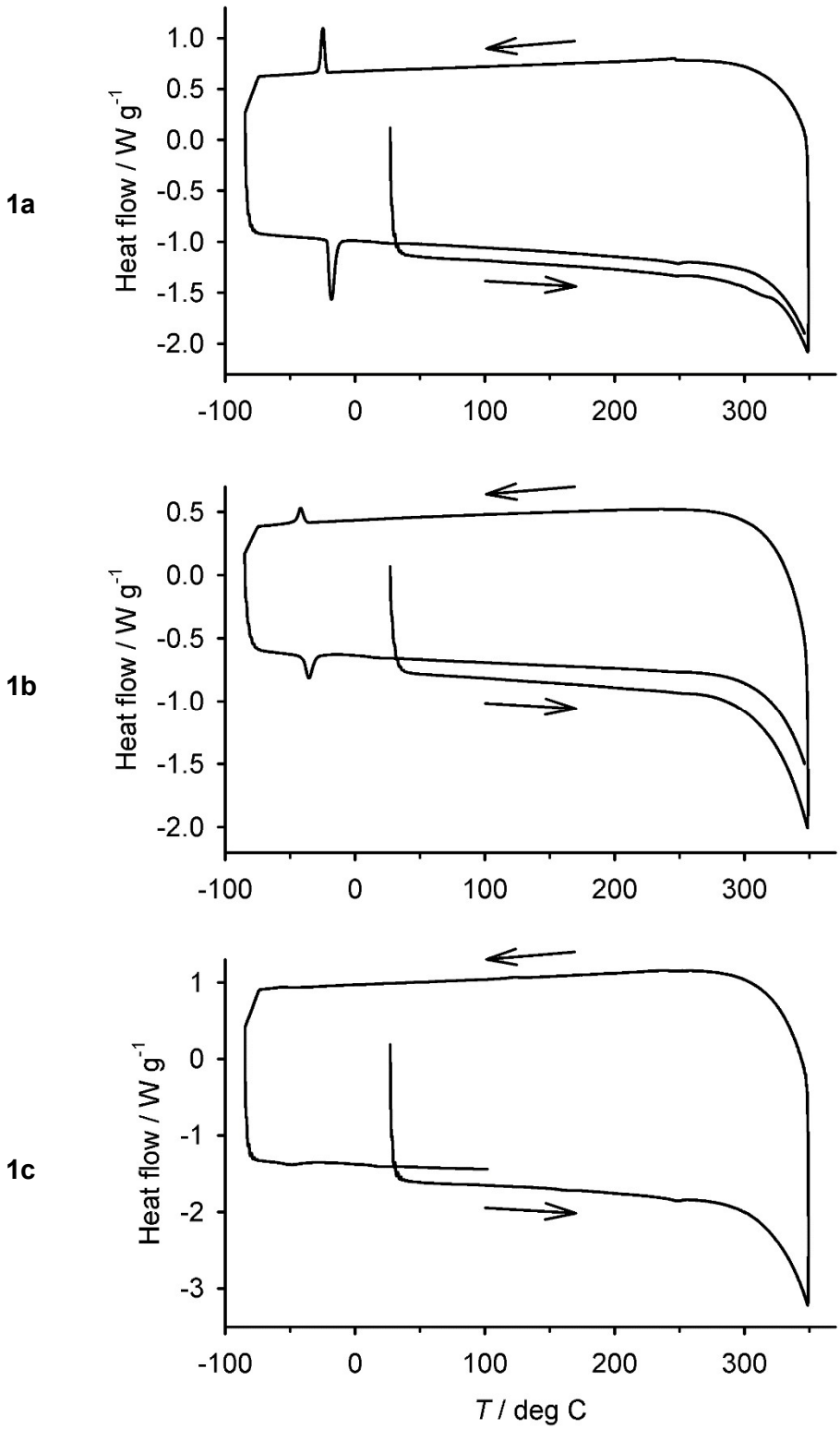

Figure S6 Differential scanning calorimetry (DSC) data for **1a**-**1c**, on a 27→350→−85→27 °C temperature cycle measured at 10 K min^{-1}.

Endotherm/exotherm features arising from SCO in **1c** are expected near −56 °C (217 K), but are not unambiguously observed. Evidently Δ*H* for SCO in **1c** is too weak to be measured by our calorimeter. For that reason **1d** and **1e**, whose endotherms would be even weaker, were not measured.

Data for the parent complex $[Fe(bpp)_2][BF_4]_2$ measured under the same conditions are presented in ref. 11.

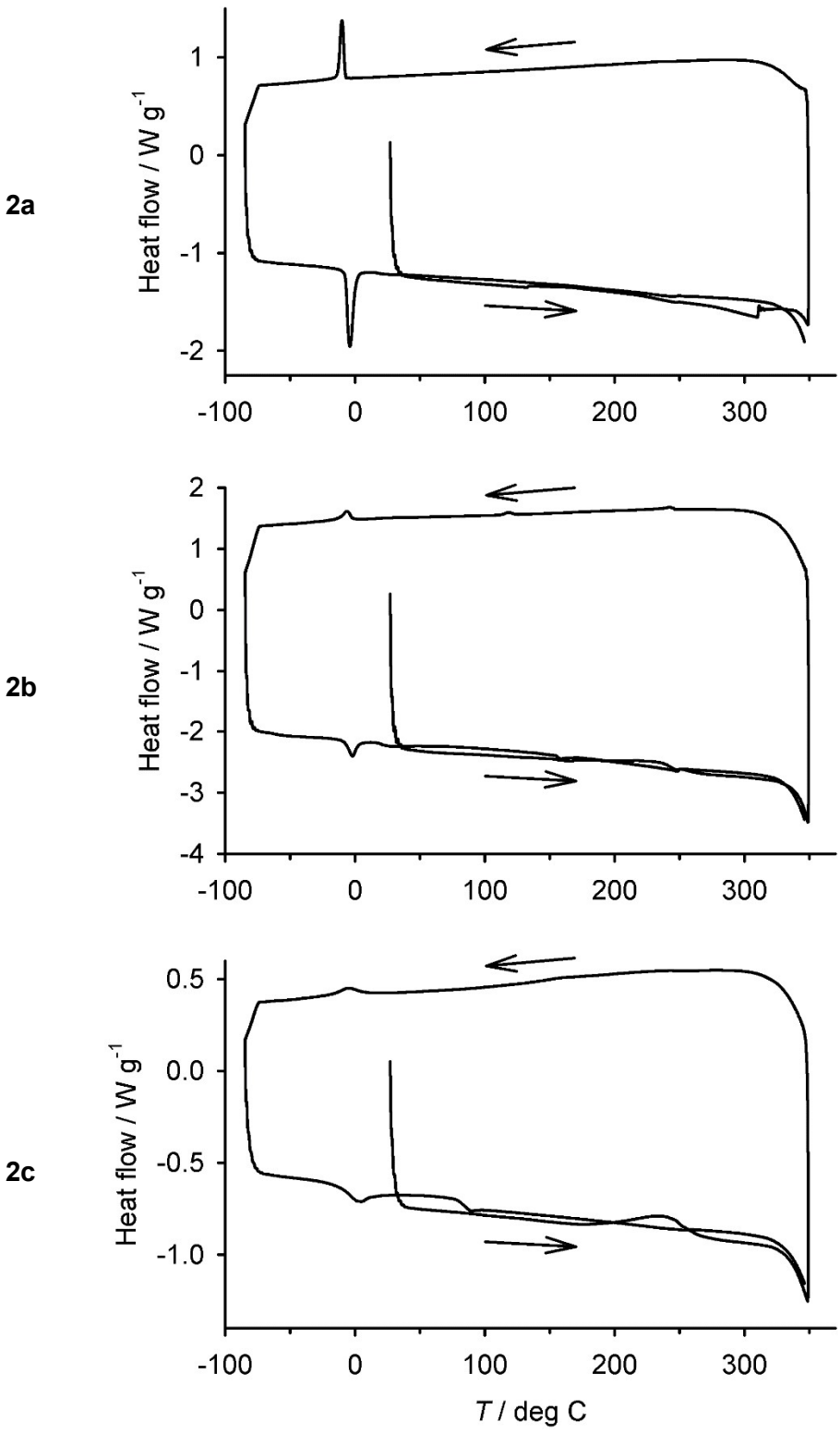

Figure S7 Differential scanning calorimetry (DSC) data for **2a**-**2c**. Details as for Figure S6.

Single Crystal Structure Analyses

Experimental details of the structure determinations are given in Table S2. All the structures were solved by direct methods *(SHELX-TL*[12]), and developed by least-squares refinement on F^2 (*SHELXL-2018*[13]). Crystallographic figures were produced using *XSEED*,[14] and other publication materials were prepared with *OLEX*2.[15]

Data at different temperatures were collected from the same crystal of each sample. The mixed-metal composition of each crystal was refined crystallographically using the disordered cation model, then the same composition was applied to the other refinements of each compound.

Disordered anions were treated with refined B–F and F···F distance restraints. All non-H atoms were refined anisotropically, except for the following two cases. First, the partial F atoms in the highly disordered BF_4^- ions were refined isotropically in the higher temperature refinement of each crystal. Second, many of the partial C and N atoms in the whole moelcule cation disorder models became non-positive definite when refined anisotropically, so those were left isotropic in the final analysis. H atoms were placed in calculated positions and refined using a riding model

Structure refinements of 1c. Two datasets were measured from the same crystal of this compound, at 100 K (low-spin) and 300 K (high-spin). Both datasets were initially refined using a single crystallographically ordered metal complex site, with a $Fe_{0.50}/Zn_{0.50}$ mixed-metal site containing partial iron and zinc atoms with the same atomic coordinates and displacement parameters. This was changed to a $Fe_{0.54}/Zn_{0.46}$ metal composition in the final least squares refinement cycles, following the disorder refinement described below.

At 100 K, the F atoms of one BF_4^- ion were disordered over two orientations, with refined occupancies of 0.67:0.33. The F atoms of both anions were modelled over three disorder sites at 300 K, with occupancies of 0.50:0.25:0.25.

After the main features of the model had been resolved, a second refinement of the 100 K dataset was performed using discrete partial (low-spin) $[Fe(bpp)_2]^{2+}$ and $[Zn(bpp)_2]^{2+}$ molecule sites, which refined successfully without restraints. The Fe:Zn occupancy ratio refined to 0.54:0.46 so those occupancies were used for those disorder sites in the final least squares cycles. The 100 K anion refinement protocol in the previous paragraph was also applied to this model.

Structure refinements of 2c. Three datasets were measured from the same crystal, at 100 K (low-spin), 200 K (low-spin) and 350 K (high-spin). These were refined as described above, using a $Fe_{0.50}/Ru_{0.50}$ mixed metal site. The F atoms of both anions were modelled over three disorder sites at 350 K, with occupancies of 0.50:0.25:0.25. No anion disorder is present in either of the low-spin refinements.

As above, the 100 K structure was also modelled using separate $[Fe(bpp)_2]^{2+}$ and $[Ru(bpp)_2]^{2+}$ molecule sites, whose occupancies refined to 0.50:0.50. The disorder model was constructed using C–C and C–N distance restraints in the partial bpp ligands, but these were removed in the final least squares cycles. However, *SIMU* restraints were applied to the disorder sites of three C atoms in the final model, whose U_{iso} values tended to correlate with each other.

Structure refinements of 3c. Three datasets were measured from one crystal of this compound, at 100 K (low-spin), 200 K (low-spin) and 350 K (high-spin). These were refined as described for **1c**, with a $Fe_{0.46}/Ni_{0.54}$ mixed metal site. The F atoms of both anions were modelled over three disorder sites at 350 K, with occupancies of 0.50:0.25:0.25. At 200 K, just one BF_4^- ion is disordered, over two sites by rotation about a B–F bond. The anions in the 100 K refinement are both crystallographically ordered.

As before, separate $[Fe(bpp)_2]^{2+}$ and $[Ni(bpp)_2]^{2+}$ molecule sites were also constructed using the 100 K dataset, whose occupancies refined to 0.46:0.54. No distance restraints were used in the final least squares cycles, but a *SIMU* restraint between the Fe and Ni atoms was required before the refinement would fully converge.

A minor merohedral twin domain was included in the refinements of **3c**, to account for its slightly high Flack parameter at 100 K.

Table S2 Experimental data for the crystal structure determinations in this work. All data were collected using synchrotron radiation (λ = 0.6889 Å). The italicised refinement parameters in brackets are from the whole-molecule cation disorder refinements of the 100 K datasets.

	1c		**2c**		
molecular formula	$C_{22}H_{18}B_2F_8Fe_{0.53}N_{10}Zn_{0.47}$		$C_{22}H_{18}B_2F_8Fe_{0.50}N_{10}Ru_{0.50}$		
M_r	656.41		674.54		
crystal class	monoclinic		monoclinic		
space group	$P2_1$		$P2_1$		
Z	2		2		
T / K	300	100	350	200	100
a / Å	8.5002(1)	8.4486(1)	8.5460(1)	8.4842(1)	8.4455(1)
b / Å	8.5263(1)	8.4867(1)	8.5956(1)	8.5569(1)	8.5114(1)
c / Å	19.0498(1)	18.5535(1)	18.9251(2)	18.4642(1)	18.4035(1)
α / °	–	–	–	–	–
β / °	95.740(1)	97.618(1)	95.794(1)	97.843(1)	98.071(1)
γ / °	–	–	–	–	–
V / Å^3	1373.72(2)	1318.56(2)	1383.10(3)	1327.93(2)	1309.80(2)
μ [λ = 0.6889 Å] / mm^{-1}	0.735	0.766	0.596	0.621	0.629
D_c / gcm^{-3}	1.587	1.653	1.620	1.687	1.710
measured reflections	14617	29979	17097	30473	30092
independent reflections	5179	12312	6919	12455	12265
R_{int}	0.086	0.047	0.040	0.050	0.068
parameters	413	425 (*402*)	413	388	388 (*365*)
restraints	61	64 (*44*)	61	1	1 (*4*)
R_1 [$F_0 > 4\sigma(F_0)$][a]	0.047	0.038 (*0.038*)	0.050	0.045	0.043 (*0.044*)
wR_2, all data[b]	0.137	0.076 (*0.075*)	0.142	0.103	0.089 (*0.089*)
goodness of fit	1.102	1.029 (*1.022*)	1.094	1.034	1.034 (*1.037*)
$\Delta\rho_{min/max}$ / *e*Å^{-3}	−0.31/0.34	−0.48/0.33 (*−0.36/0.30*)	−0.28/0.33	−0.45/0.56	−0.55/0.70 (*−0.56/0.65*)
Flack parameter	−0.014(15)	−0.004(5) (*−0.006(5)*)	−0.025(19)	−0.036(12)	−0.005(12) (*−0.005(12)*)
CCDC	2261786	2261787 (*2261788*)	2261789	2261790	2261791 (*2261792*)

[a] $R = \Sigma[\,|F_o| - |F_c|\,] / \Sigma|F_o|$ [b] $wR = [\Sigma w(F_o^2 - F_c^2) \;/\; \Sigma wF_o^4]^{1/2}$ [c] A minor inversion twin domain was included in the refinement, to account for the slightly high Flack parameter at 100 K.

Table S2 continued

	3c		
molecular formula	$C_{22}H_{18}B_2F_8Fe_{0.46}N_{10}Ni_{0.54}$		
M_r	653.48		
crystal class	monoclinic		
space group	$P2_1$		
Z	2		
T / K	350	200	100
a / Å	8.5413(1)	8.4832(1)	8.4441(1)
b / Å	8.5895(1)	8.5546(1)	8.5062(1)
c / Å	18.9944(2)	18.5399(1)	18.4578(1)
α / °	–	–	–
β / °	95.702(1)	97.609(1)	97.907(1)
γ / °	–	–	–
V / Å^3	1386.64(3)	1333.60(2)	1313.17(2)
μ [λ = 0.6889 Å] / mm^{-1}	0.660	0.687	0.697
D_c / gcm^{-3}	1.565	1.627	1.653
measured reflections	17249	30659	30085
independent reflections	6811	12471	12239
R_{int}	0.054	0.052	0.049
parameters	414	417	389 (*366*)
restraints	61	55	1 (*7*)
R_1 [$F_0 > 4\sigma(F_0)$][a]	0.062	0.048	0.040 (*0.041*)
wR_2, all data[b]	0.204	0.103	0.091 (*0.092*)
goodness of fit	1.187	1.052	1.021 (*1.018*)
$\Delta\rho_{min/max}$ / eÅ^{-3}	−0.42/0.34	−0.37/0.53	−0.50/0.54 (*−0.38/0.55*)
Flack parameter	0.02(3)[c]	0.018(13)[c]	0.056(10)[c] (*0.057(10)*[c])
CCDC	2261793	2261794	2261795 (*2261796*)

[a] $R = \Sigma[||F_o| - |F_c||] / \Sigma|F_o|$ [b] $wR = [\Sigma w(F_o^2 - F_c^2) \ / \ \Sigma wF_o^4]^{1/2}$ [c] A minor inversion twin domain was included in the refinement, to account for the slightly high Flack parameter at 100 K.

Definitions of the Structural Parameters in Tables S3-S5

Θ is defined as follows:

$$\Theta = \sum_{i=1}^{24} 60\text{-}\beta_i$$

where β_i are the 24 unique N–Fe–N angles measured on the projection of two triangular faces of the octahedron along their common pseudo-threefold axis (Scheme S1). Θ indicates the distortion of a formally octahedral metal ion towards a trigonal prismatic structure. A perfectly octahedral complex gives $\Theta = 0$.[16,17]

Because the high-spin state of a complex has a much more plastic structure than the low-spin, this is reflected in Θ which is usually much larger in the high-spin state. The absolute values of these parameters depend on the metal/ligand combination in the compound under investigation, however.[18]

The change in Θ during SCO is an important contributor to $T_{½}$, in materials that are isomorphous or adopt similar modes of crystal packing.[19,20] We recently showed that correlation operates for $[Fe(bpp)_2]^{2+}$ complex salts, with the terpyridine embrace lattice type.[20] That is discussed in the main article.

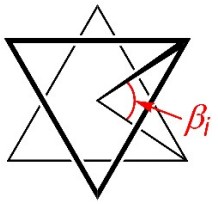

Scheme S1 Angles used in the definition of the coordination distortion parameter Θ.

The *trans*-N{pyridyl}–Fe–N{pyridyl} bond angle, ϕ, is also mentioned in the main article (Scheme S2). $\phi = 180°$ in the idealised D_{2d} molecular symmetry for $[Fe(bpp)_2]^{2+}$ derivatives but it can deviate significantly from that value, particularly in the high-spin state.[21] Large changes in ϕ between the spin states can lead to highly cooperative spin-transitions.[22]

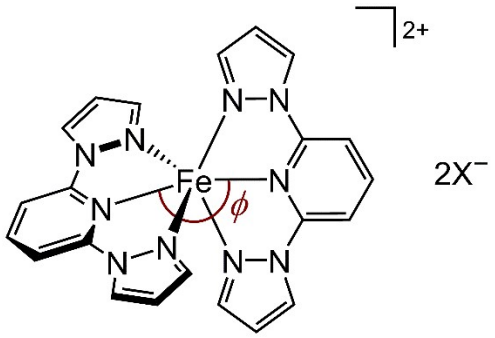

Scheme S2 The distortion parameter ϕ.

The average chelate bite angle of the bpp ligands in the molecules, γ, is also listed in Table 3. This the average of the four intra-ligand *cis*-N{pyridyl}–Fe–N{pyrazolyl} bond angles in each crystal structure. In pure $[Fe(bpp)_2]^{2+}$ derivatives γ is *ca* 73° in the high spin state, and 80° in the low-spin state.[21] However γ is very sensitive to small changes in spin state population, or the presence of dopant molecules.

[This bite angle parameter is often labelled 'α' in the literature, but we used 'γ' in this paper to avoid confusion with the α_i thermal expansion parameters].

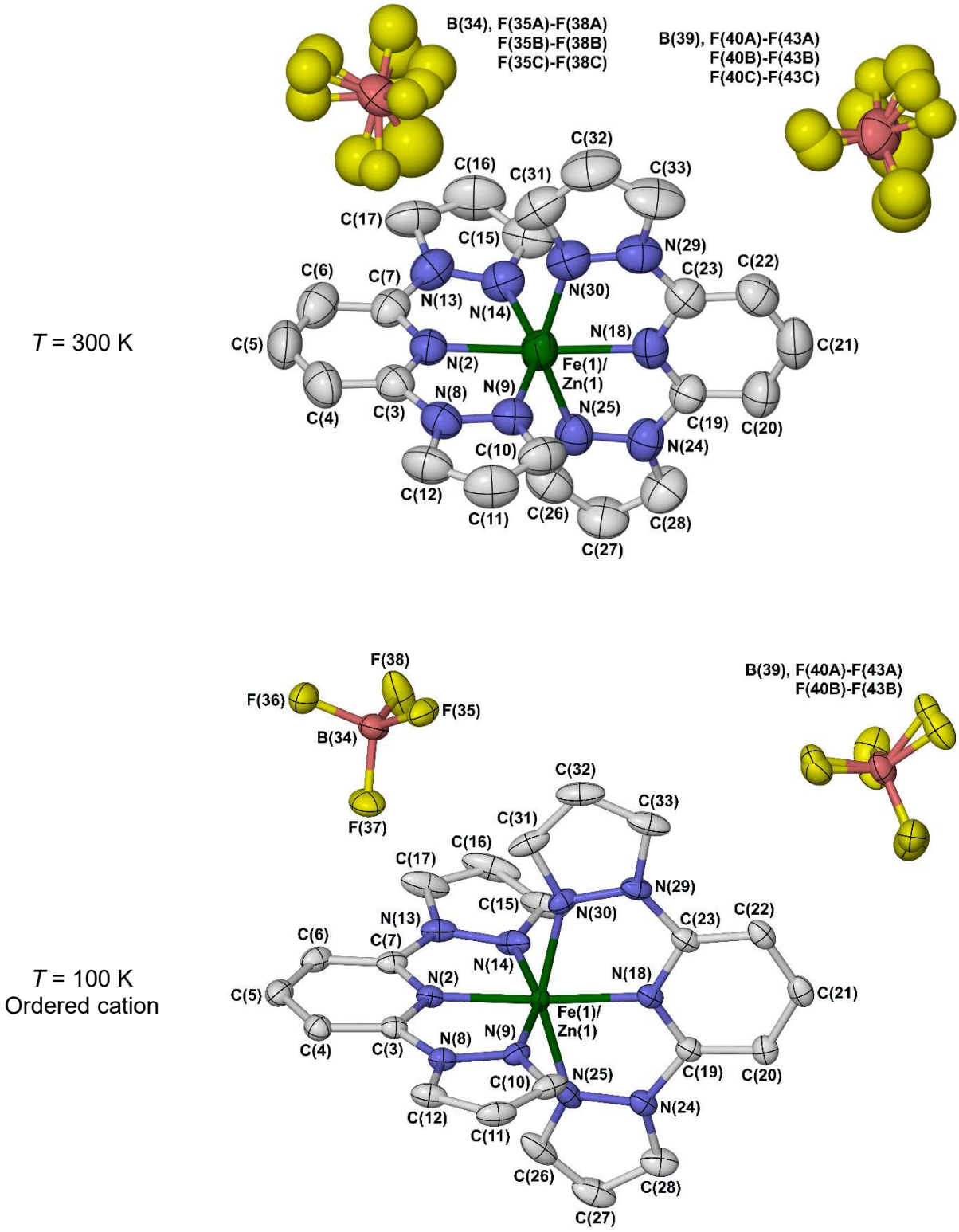

Figure S8 The asymmetric unit of **1c** at 300 K (top) and 100 K (bottom), in the ordered cation refinement. Displacement ellipsoids are at the 50 % probability level, and H atoms are omitted for clarity.

Colour code: C, white; B, pink; F, yellow; Fe/Zn, dark green; N, blue.

T = 100 K
Disordered cation

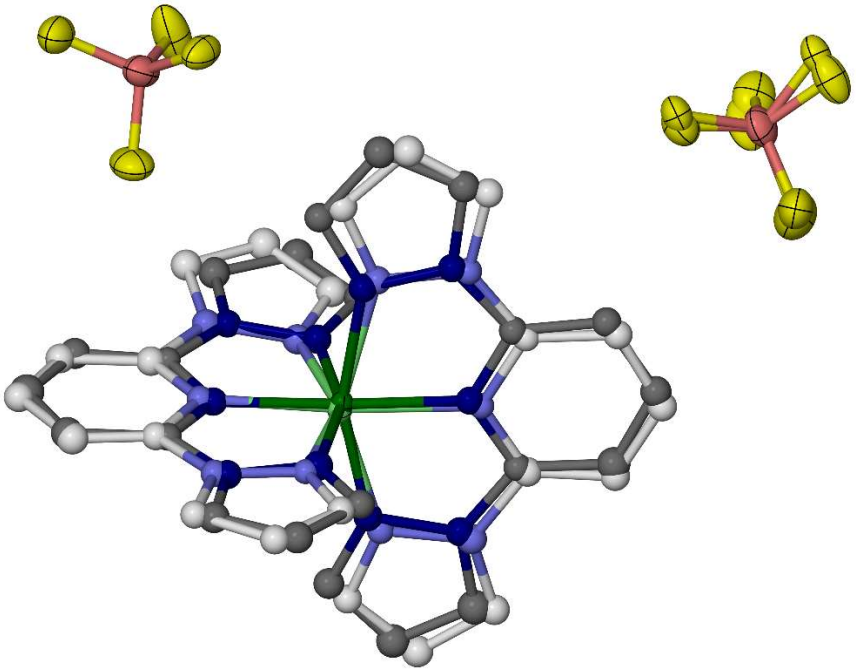

Figure S8 continued.

The partial $[Fe(bpp)_2]^{2+}$ and $[Zn(bpp)_2]^{2+}$ cation sites in the disordered low temperature refinement are distinguished with dark and pale colouration, respectively. No crystallographic restraints were applied to the final least squares cycles of the disorder model. The atom numbering for this model is the same as on the previous page, with 'A' and 'B' suffixes denoting atoms from the iron and zinc complex molecules.

Colour code: C, white or dark grey; B, pink; F, yellow; Fe, dark green; N, pale or dark blue; Zn, pale green.

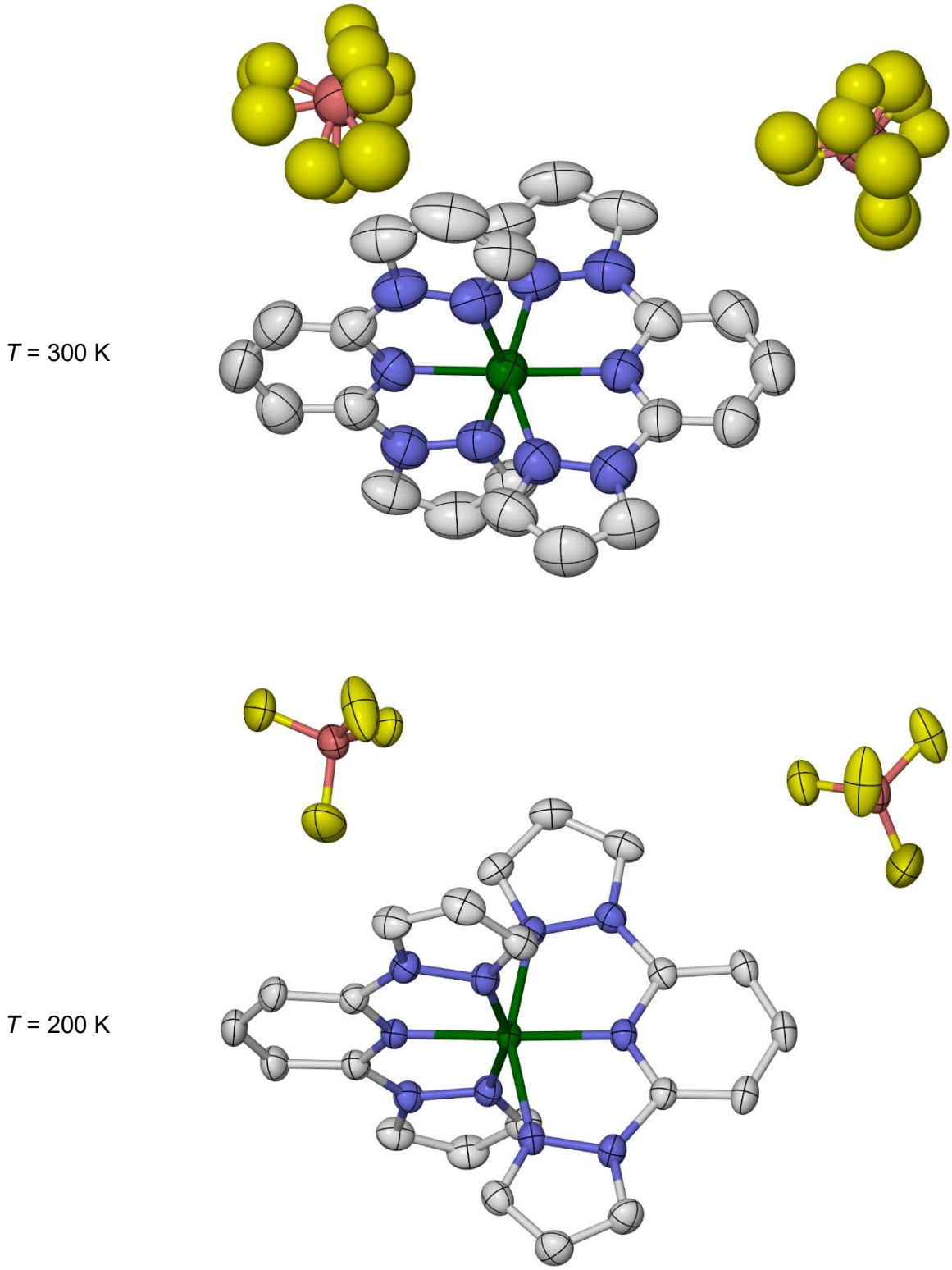

Figure S9 The asymmetric unit of **2c** at 300 K (top), 200 K (bottom) and the two 100 K refinements (next page). Displacement ellipsoids are at the 50 % probability level, and H atoms are omitted for clarity. The atom numbering scheme is the same as in Figure S8, with Zn(1) replaced by Ru(1).

Colour code: C, white; B, pink; F, yellow; Fe/Ru, green; N, blue.

This crystal is the opposite handedness compared to the crystal of **1c** (Figure S8), in the chiral $P2_1$ space group.

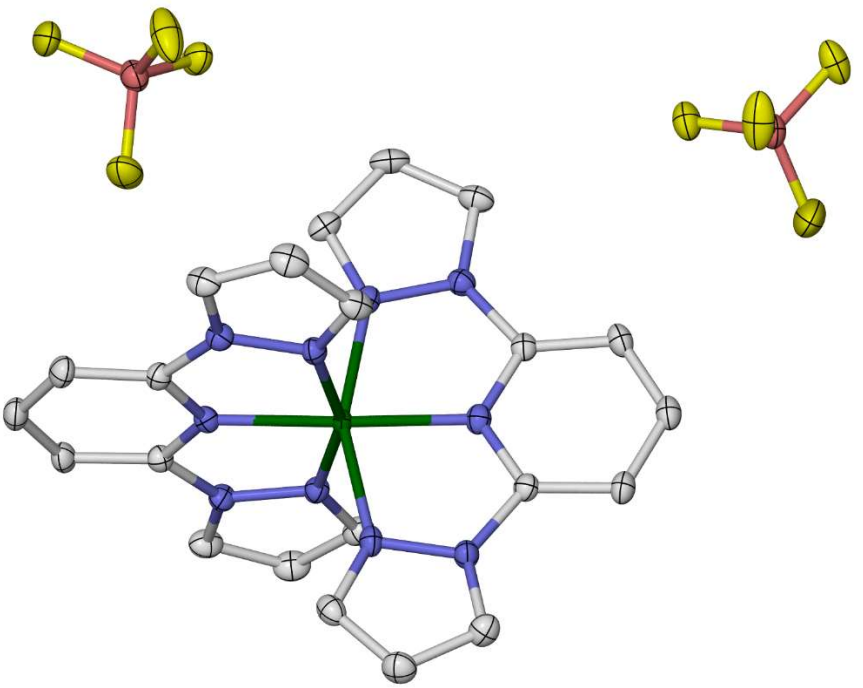

T = 100 K
Ordered cation

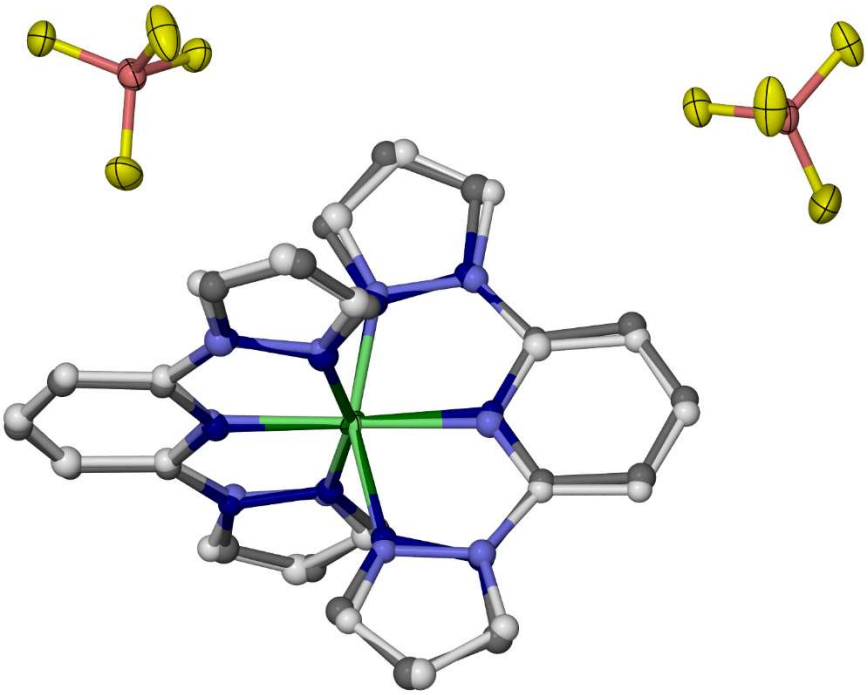

T = 100 K
Disordered cation

Figure S9 continued.

The partial $[Fe(bpp)_2]^{2+}$ and $[Ru(bpp)_2]^{2+}$ cation sites in the disordered low temperature refinement are distinguished with dark and pale colouration, respectively. No distance restraints were applied to the final least squares cycles of the disorder model, but the U_{iso} displacement parameters of three pairs of partial C atoms in the model were constrained to be similar with a *SIMU* instruction.

Colour code: C, white or dark grey; B, pink; F, yellow; Fe, dark green; N, pale or dark blue; Ru, pale green.

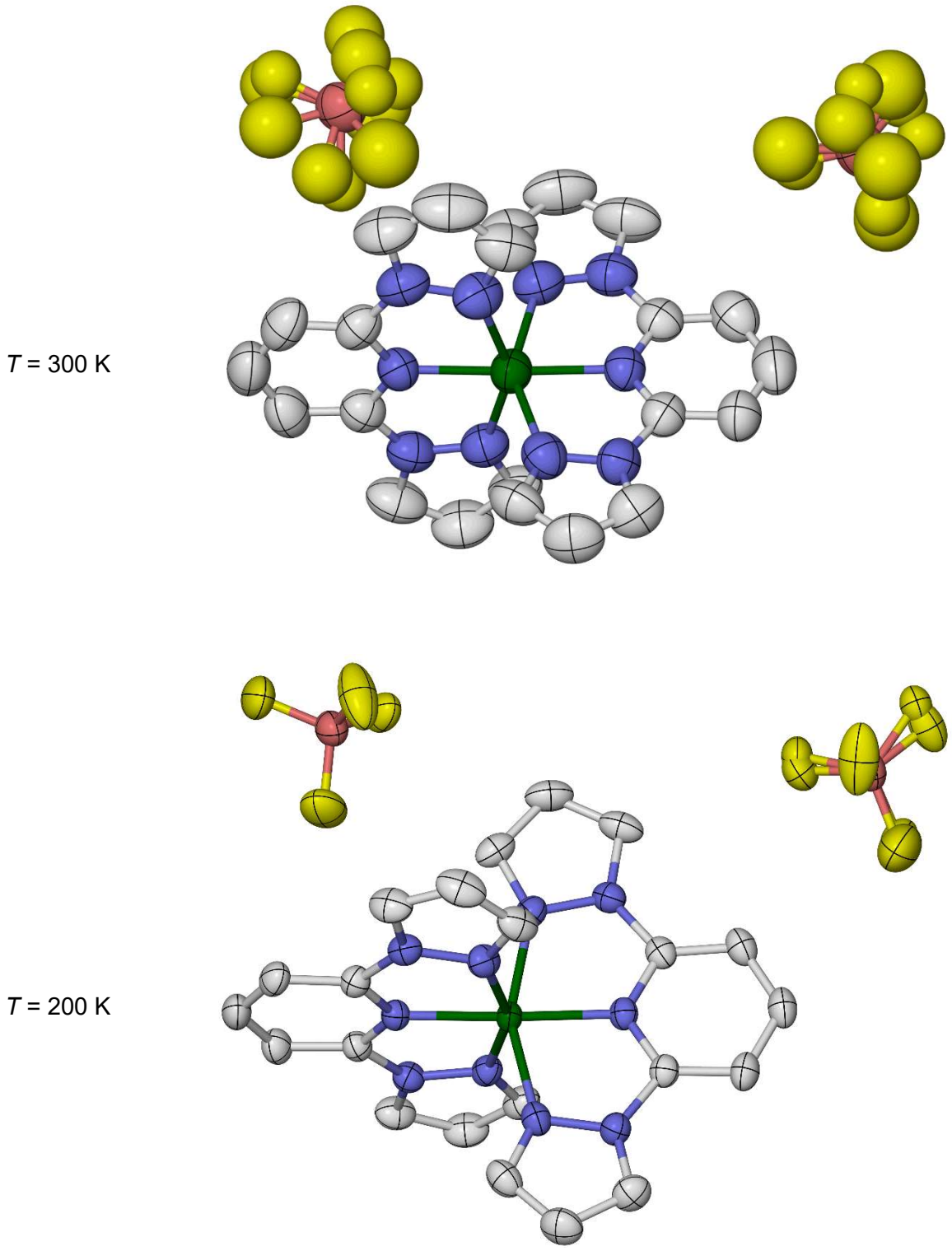

Figure S10 The asymmetric unit of **3c** at 300 K (top), 200 K (bottom) and 100 K (next page), in the ordered cation refinement. Displacement ellipsoids are at the 50 % probability level, and H atoms are omitted for clarity. The atom numbering scheme is the same as in Figure S8, with Zn(1) replaced by Ni(1).

Colour code: C, white; B, pink; F, yellow; Fe/Ni, dark green; N, blue.

This crystal is the same handedness as the crystal of **2c** (Figure S9) in the chiral $P2_1$ space group, but has the opposite handedness to the crystal of **1c** (Figure S8).

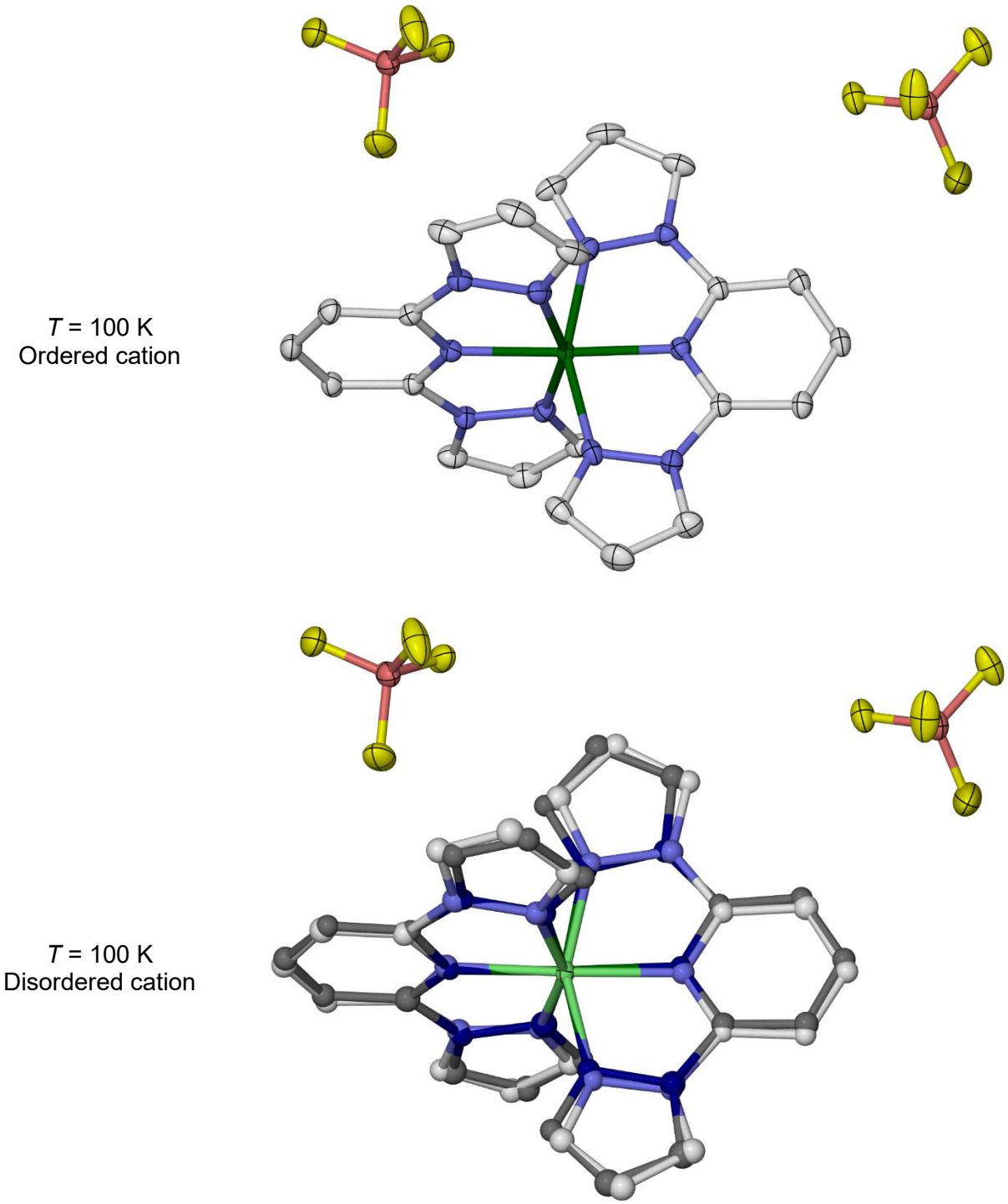

Figure S10 continued.

The partial $[Fe(bpp)_2]^{2+}$ and $[Ni(bpp)_2]^{2+}$ cation sites in the disordered low temperature refinement are distinguished with dark and pale colouration, respectively. No distance restraints were applied to the final least squares cycles of the disorder model, but the U_{eq} displacement parameters of the partial Fe and Ni atoms correlated in the refinement and were hence constrained to be similar with a *SIMU* instruction.

Colour code: C, white or dark grey; B, pink; F, yellow; Fe, dark green; N, pale or dark blue; Ni, pale green.

Table S3 Selected crystallographic bond lengths (Å) and angles (°) for **1c**. See Figure S8 for the atom numbering scheme. Data in square brackets are from the low-spin $[Fe(bpp)_2][BF_4]_2$[8] and $[Zn(bpp)_2][BF_4]_2$[9] precursor crystals at 150 K, which are included for comparison. Italicised parameters in curly brackets are weighted average values, calculated from the appropriate spin state of $[Fe(bpp)_2][BF_4]_2$ and the dopant complex.

	T = 100 K, disordered cation		T = 100 K, ordered cation	T = 300 K
	M = Fe (molecule A)	M = Zn (molecule B)	M = Fe, Zn	M = Fe, Zn
M(1)–N(2)	1.912(7) [1.9001(16)]	2.088(7) [2.104(3)]	1.9934(15) {*1.994(3)*}	2.113(4) {*2.116(4)*}
M(1)–N(9)	1.986(7) [1.9860(18)]	2.187(7) [2.185(3)]	2.0830(18) {*2.078(3)*}	2.195(5) {*2.197(4)*}
M(1)–N(14)	1.967(7) [1.9682(18)]	2.159(7) [2.160(3)]	2.048(2) {*2.056(3)*}	2.171(5) {*2.166(5)*}
M(1)–N(18)	1.906(7) [1.9029(17)]	2.102(7) [2.097(3)]	1.9992(15) {*1.992(3)*}	2.115(4) {*2.112(4)*}
M(1)–N(25)	1.968(9) [1.9880(19)]	2.186(9) [2.184(4)]	2.064(2) {*2.078(4)*}	2.180(5) {*2.180(5)*}
M(1)–N(30)	1.986(10) [1.9701(19)]	2.179(10) [2.176(4)]	2.0748(18) {*2.065(4)*}	2.191(5) {*2.182(6)*}
M(1)–N{pyridyl}$_{average}$	1.909(10) [1.902(2)]	2.095(10) [2.101(4)]	1.996(2) {*1.993(4)*}	2.114(6) {*2.114(6)*}
M(1)–N{pyrazolyl}$_{average}$	1.977(17) [1.983(4)]	2.177(17) [2.176(7)]	2.067(3) {*2.069(5)*}	2.184(10) {*2.181(10)*}
N(2)–M(1)–N(9)	79.4(3) [79.90(7)]	74.6(3) [74.15(12)]	76.96(6) {*77.26(14)*}	73.62(16) {*73.68(16)*}
N(2)–M(1)–N(14)	79.7(3) [80.16(7)]	74.7(3) [74.57(12)]	77.43(7) {*77.59(14)*}	73.97(17) {*74.00(17)*}
N(2)–M(1)–N(18)	176.9(6) [178.00(9)]	174.1(5) [172.99(15)]	175.47(8) {*175.70(17)*}	173.8(2) {*173.5(2)*}
N(2)–M(1)–N(25)	103.1(4) [101.94(8)]	111.2(4) [111.98(14)]	107.12(7) {*106.56(16)*}	111.9(2) {*112.2(2)*}
N(2)–M(1)–N(30)	97.6(4) [97.94(7)]	99.6(4) [99.41(14)]	98.54(7) {*98.62(16)*}	100.4(2) {*100.4(2)*}
N(9)–M(1)–N(14)	159.1(3) [160.06(7)]	149.3(3) [148.69(12)]	154.36(7) {*154.83(14)*}	147.58(19) {*147.64(17)*}
N(9)–M(1)–N(18)	100.5(3) [100.76(7)]	104.0(3) [103.64(12)]	102.30(6) {*102.08(14)*}	103.74(17) {*103.78(17)*}
N(9)–M(1)–N(25)	93.8(4) [93.13(7)]	97.1(3) [97.95(13)]	95.40(7) {*95.35(15)*}	97.21(18) {*97.67(18)*}
N(9)–M(1)–N(30)	91.0(3) [92.14(7)]	93.7(3) [92.80(12)]	92.26(7) {*92.44(14)*}	93.12(18) {*92.95(17)*}
N(14)–M(1)–N(18)	100.3(3) [99.16(7)]	106.5(3) [107.25(12)]	103.12(7) {*102.88(14)*}	108.41(18) {*108.19(17)*}
N(14)–M(1)–N(25)	92.4(3) [91.41(8)]	94.3(3) [94.90(13)]	93.31(7) {*93.02(15)*}	95.57(18) {*95.72(17)*}
N(14)–M(1)–N(30)	90.2(3) [90.15(7)]	90.9(3) [90.91(13)]	90.24(7) {*90.50(15)*}	91.81(19) {*91.46(19)*}
N(18)–M(1)–N(25)	80.0(3) [79.93(7)]	74.6(3) [74.79(13)]	77.37(7) {*77.57(15)*}	73.8(2) {*73.90(19)*}
N(18)–M(1)–N(30)	79.3(3) [80.16(7)]	74.7(3) [73.93(14)]	76.99(7) {*77.29(16)*}	73.9(2) {*73.5(2)*}
N(25)–M(1)–N(30)	159.3(4) [160.03(7)]	149.0(3) [148.51(12)]	154.26(7) {*154.73(14)*}	147.62(18) {*147.28(17)*}
Θ^{a}	294.1(16) [282]	436.0(18) [443]	362.8(6) {*356*}	457.2(17) {*456*}

[a]Defined on page S15.

There is an excellent structural correspondence between low-spin $[Fe(bpp)_2]^{2+}$ and $[Zn(bpp)_2]^{2+}$ in the disordered cation refinement, and their counterparts in the single-component crystals $[Fe(bpp)_2][BF_4]_2$ and $[Zn(bpp)_2][BF_4]_2$. Co-crystallisation of those cations has no effect on their molecular geometry, within the accuracy of the measurement.

Table S4 Selected crystallographic bond lengths (Å) and angles (°) for **2c**. The atom numbering is equivalent to that in Figure S8, with Ru(1) replacing Zn(1) as appropriate. Data in square brackets are from the low-spin $[Fe(bpp)_2][BF_4]_2$[8] and $[Ru(bpp)_2][BF_4]_2$[10] precursor crystals at 150 K, which are included for comparison. Italicised parameters in curly brackets are weighted average values, calculated from the appropriate spin state of $[Fe(bpp)_2][BF_4]_2$ and the dopant complex.

	T = 100 K, disordered cation		T = 100 K, ordered cation[a]	T = 350 K
	M = Fe (molecule A)	M = Ru (molecule B)	M = Fe, Ru	M = Fe, Ru
M(1)–N(2)	1.915(11) [1.9001(16)]	1.976(10) [2.023(2)]	1.9464(18) {*1.962(3)*}	2.055(4) {*2.074(3)*}
M(1)–N(9)	1.974(11) [1.9860(18)]	2.088(10) [2.103(3)]	2.033(2) {*2.045(3)*}	2.130(5) {*2.148(4)*}
M(1)–N(14)	1.956(11) [1.9682(18)]	2.060(10) [2.081(3)]	2.015(2) {*2.025(3)*}	2.110(6) {*2.128(4)*}
M(1)–N(18)	1.966(9) [1.9029(17)]	1.939(9) [2.022(3)]	1.9528(19) {*1.962(3)*}	2.060(4) {*2.075(4)*}
M(1)–N(25)	1.951(9) [1.9880(19)]	2.125(8) [2.095(3)]	2.038(2) {*2.042(4)*}	2.134(6) {*2.140(4)*}
M(1)–N(30)	1.953(11) [1.9701(19)]	2.076(11) [2.079(3)]	2.019(2) {*2.025(4)*}	2.103(6) {*2.132(4)*}
M(1)–N{pyridyl}$_{average}$	1.941(14) [1.902(2)]	1.958(13) [2.023(4)]	1.950(3) {*1.962(4)*}	2.058(6) {*2.074(5)*}
M(1)–N{pyrazolyl}$_{average}$	1.96(2) [1.983(4)]	2.09(2) [2.090(6)]	2.026(4) {*2.034(7)*}	2.119(12) {*2.137(8)*}
N(2)–M(1)–N(9)	78.6(5) [79.90(7)]	79.4(4) [78.41(11)]	79.03(8) {*79.16(13)*}	75.9(2) {*75.94(14)*}
N(2)–M(1)–N(14)	80.1(5) [80.16(7)]	78.2(4) [78.35(11)]	79.10(8) {*79.26(13)*}	75.9(2) {*76.00(14)*}
N(2)–M(1)–N(18)	177.3(5) [178.00(9)]	179.2(6) [178.26(19)]	177.94(11) {*178.1(2)*}	177.6(3) {*175.7(2)*}
N(2)–M(1)–N(25)	102.2(5) [101.94(8)]	103.7(4) [103.82(14)]	103.09(9) {*102.88(16)*}	107.2(3) {*108.48(17)*}
N(2)–M(1)–N(30)	99.6(5) [97.94(7)]	98.3(5) [99.83(13)]	98.88(9) {*98.89(15)*}	101.2(3) {*100.02(16)*}
N(9)–M(1)–N(14)	158.7(5) [160.06(7)]	157.5(4) [156.73(10)]	158.11(8) {*158.40(12)*}	151.8(2) {*151.91(13)*}
N(9)–M(1)–N(18)	101.9(4) [100.76(7)]	101.2(4) [102.13(11)]	101.59(8) {*101.45(13)*}	103.6(2) {*103.19(14)*}
N(9)–M(1)–N(25)	94.1(5) [93.13(7)]	93.8(4) [94.46(11)]	93.87(9) {*93.80(13)*}	94.9(2) {*96.46(14)*}
N(9)–M(1)–N(30)	91.9(5) [92.14(7)]	92.6(4) [92.54(11)]	92.29(9) {*92.34(13)*}	93.9(2) {*92.71(14)*}
N(14)–M(1)–N(18)	99.3(4) [99.16(7)]	101.2(4) [101.06(11)]	100.23(8) {*100.11(13)*}	104.6(2) {*104.64(14)*}
N(14)–M(1)–N(25)	90.9(5) [91.41(8)]	92.9(4) [92.16(12)]	92.02(9) {*91.79(14)*}	93.7(2) {*94.04(15)*}
N(14)–M(1)–N(30)	91.2(5) [90.15(7)]	89.2(4) [90.29(12)]	90.10(9) {*90.22(14)*}	91.2(2) {*90.71(16)*}
N(18)–M(1)–N(25)	80.5(4) [79.93(7)]	76.8(4) [77.82(13)]	78.85(9) {*78.88(15)*}	75.1(2) {*75.63(16)*}
N(18)–M(1)–N(30)	77.8(4) [80.16(7)]	81.2(4) [78.51(13)]	79.15(9) {*79.34(15)*}	76.4(3) {*75.91(16)*}
N(25)–M(1)–N(30)	158.2(4) [160.03(7)]	157.9(4) [156.23(10)]	157.93(8) {*158.13(12)*}	151.5(2) {*151.41(13)*}
Θ[b]	300(4) [282]	321(4) [332]	308.7(9) {*307*}	400(2) {*400*}

[a]The metric parameters from the 200 K refinement of this crystal are identical to the 100 K structure, within experimental error. [b]Defined on page S15.

This disordered cation analysis shows the greatest structural variation in the iron and ruthenium centres, between the doped compound and the corresponding precursor crystals. That should reflect that the geometry of the $[Ru(bpp)_2]^{2+}$ dopant in **2c** is most similar to that of low-spin $[Fe(bpp)_2]^{2+}$, so the two components are less well distinguished by the disorder model. The greatest discrepancies occur in bonds and angles involving the pyridyl ligand donor atoms, N(2) and N(18).

Table S5 Selected crystallographic bond lengths (Å) and angles (°) for **3c**. The atom numbering is equivalent to that in Figure S8, with Ni(1) replacing Zn(1) as appropriate. Data in square brackets are from the low-spin $[Fe(bpp)_2][BF_4]_2$[8] and $[Ni(bpp)_2][BF_4]_2$[23] precursor crystals at 150 K, which are included for comparison. Italicised parameters in curly brackets are weighted average values, calculated from the appropriate spin state of $[Fe(bpp)_2][BF_4]_2$ and the dopant complex.

	T = 100 K, disordered cation		T = 100 K, ordered cation[a]	T = 350 K
	M = Fe (molecule A)	M = Ni (molecule B)	M = Fe, Ni	M = Fe, Ni
M(1)–N(2)	1.914(15) [1.9001(16)]	1.993(13) [2.0122(13)]	1.9547(17) {*1.961(2)*}	2.063(4) {*2.064(2)*}
M(1)–N(9)	1.959(16) [1.9860(18)]	2.116(12) [2.1187(16)]	2.0504(19) {*2.058(2)*}	2.149(6) {*2.153(3)*}
M(1)–N(14)	1.985(14) [1.9682(18)]	2.066(11) [2.0944(16)]	2.029(2) {*2.036(2)*}	2.132(6) {*2.131(3)*}
M(1)–N(18)	1.950(14) [1.9029(17)]	1.968(11) [2.0143(14)]	1.9582(17) {*1.963(2)*}	2.066(5) {*2.066(2)*}
M(1)–N(25)	1.974(16) [1.9880(19)]	2.114(13) [2.1229(16)]	2.051(2) {*2.061(2)*}	2.155(7) {*2.151{3}*}
M(1)–N{pyridyl}$_{average}$	1.93(2) [1.902(2)]	1.981(17) [2.0133(19)]	1.959(2) {*1.962(3)*}	2.065(6) {*2.065{3}*}
M(1)–N{pyrazolyl}$_{average}$	1.97(3) [1.983(4)]	2.10(2) [2.109(3)]	2.041(4) {*2.049(4)*}	2.144(13) {*2.144(6)*}
N(2)–M(1)–N(9)	80.7(6) [79.90(7)]	76.7(5) [76.78(6)]	78.35(7) {*78.22(9)*}	75.4(2) {*75.26(10)*}
N(2)–M(1)–N(14)	79.5(6) [80.16(7)]	77.7(5) [77.08(6)]	78.46(7) {*78.50(9)*}	75.0(2) {*75.50(11)*}
N(2)–M(1)–N(18)	177.1(10) [178.00(9)]	176.6(8) [176.95(7)]	177.32(8) {*177.43(11)*}	176.6(3) {*175.20(12)*}
N(2)–M(1)–N(25)	102.1(7) [101.94(8)]	106.2(6) [106.19(6)]	104.37(8) {*104.24(10)*}	108.8(3) {*109.39(11)*}
N(2)–M(1)–N(30)	99.8(7) [97.94(7)]	98.0(6) [99.90(6)]	98.89(8) {*99.00(9)*}	101.0(3) {*100.04(12)*}
N(9)–M(1)–N(14)	160.1(7) [160.06(7)]	154.4(5) [153.84(6)]	156.79(7) {*156.70(9)*}	150.4(2) {*150.73(11)*}
N(9)–M(1)–N(18)	101.7(6) [100.76(7)]	102.2(5) [103.21(6)]	102.08(7) {*102.08(9)*}	103.7(2) {*103.68(11)*}
N(9)–M(1)–N(25)	95.0(7) [93.13(7)]	93.8(5) [95.34(6)]	94.27(7) {*94.32(9)*}	95.5(2) {*96.78(10)*}
N(9)–M(1)–N(30)	92.0(7) [92.14(7)]	92.7(5) [92.81(6)]	92.43(8) {*92.50(9)*}	93.4(2) {*92.84(11)*}
N(14)–M(1)–N(18)	98.1(6) [99.16(7)]	103.4(5) [102.84(6)]	101.05(8) {*101.15(9)*}	105.8(2) {*105.31(11)*}
N(14)–M(1)–N(25)	90.8(6) [91.41(8)]	93.3(4) [92.85(6)]	92.25(8) {*92.19(10)*}	94.5(2) {*94.28(11)*}
N(14)–M(1)–N(30)	89.8(7) [90.15(7)]	90.8(5) [90.65(6)]	90.31(8) {*90.42(9)*}	91.6(3) {*90.87(12)*}
N(18)–M(1)–N(25)	79.5(6) [79.93(7)]	77.1(4) [76.86(6)]	78.26(7) {*78.27(9)*}	74.5(3) {*75.29(11)*}
N(18)–M(1)–N(30)	78.4(6) [80.16(7)]	78.7(5) [77.05(6)]	78.46(7) {*78.48(9)*}	75.7(3) {*75.33(12)*}
N(25)–M(1)–N(30)	157.8(7) [160.03(7)]	155.8(5) [153.81(6)]	156.64(7) {*156.67(9)*}	150.2(2) {*150.48(11)*}
Θ[b]	293(3) [282]	358(3) [373]	332.1(8) {*331*}	421(2) {*416*}

[a]The metric parameters from the 200 K refinement of this crystal are identical to the 100 K structure, within experimental error. [b]Defined on page S15.

The disordered cation refinement of **3c** is the least precise of the three compounds studied. None-the-less the $[Fe(bpp)_2]^{2+}$ and $[Ni(bpp)_2]^{2+}$ components in the doped crystal show good agreement with the pure precursor crystals, since each metric parameter is identical in the two crystals to within 4σ. As for **2c**, the M(1)–N(18) bond length shows the largest deviation from expectation, in both molecules.

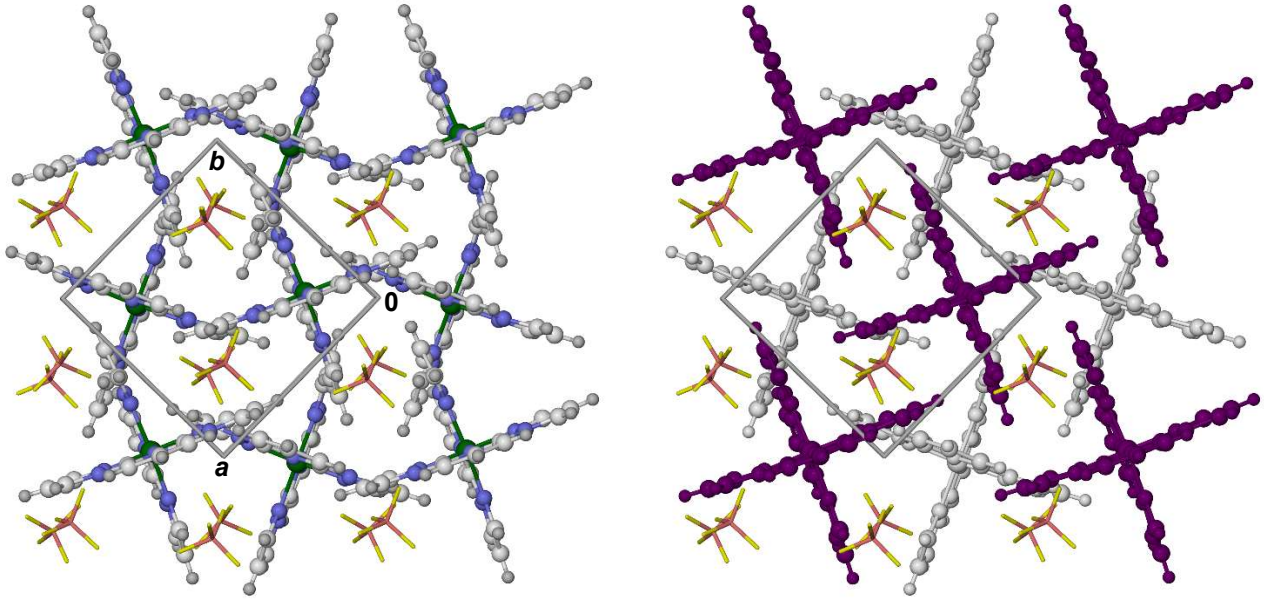

Figure S11 Packing diagrams of $[Fe(bpp)_2][BF_4]_2$[1] at 150 K viewed perpendicular to (001), which is the plane of the terpyridine embrace cation layers.[24,25] The BF_4^- ions are de-emphasised for clarity. Left: colour coded by element as below. Right: the same view, with alternate cation layers colour coded white and purple.

Element colour code: C, white; H, pale grey; B, pink; F, yellow; Fe, green; N, blue.

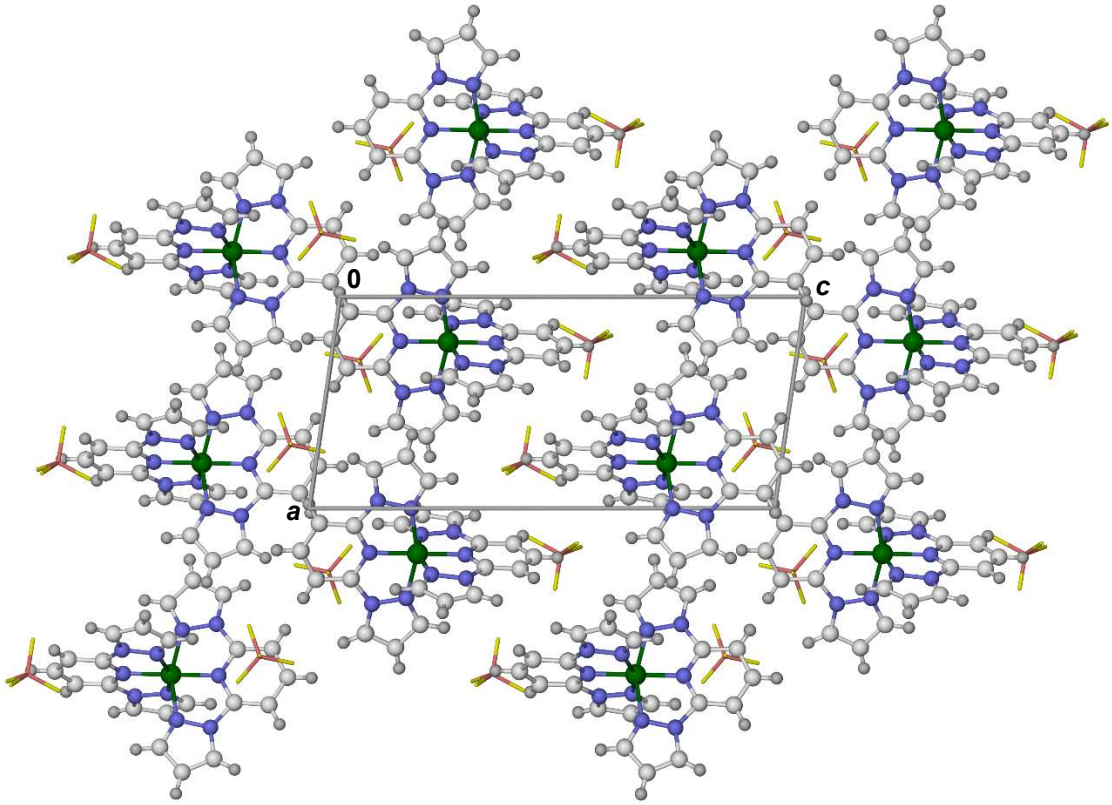

Figure S12 Packing diagram of $[Fe(bpp)_2][BF_4]_2$ at 150 K viewed perpendicular (010), within the plane of the terpyridine embrace cation layers. Details as for Figure S11. An alternative version of this view with false colouring to highlight the cation layers (as above), is given in Figure 6 (main article).

Table S6 Variable temperature single crystal unit cells for $[Fe(bpp)_2][BF_4]_2$ (monoclinic, space group $P2_1$).

T / K	a / Å	b / Å	c / Å	β / °	V / Å^3
350	8.5199(7)	8.531(2)	19.1569(15)	95.099(7)	1386.9(4)
340	8.5152(5)	8.5283(18)	19.1443(11)	95.225(5)	1384.5(3)
330	8.5108(5)	8.5202(17)	19.1265(11)	95.314(5)	1381.0(3)
320	8.5082(5)	8.5161(17)	19.1093(10)	95.429(5)	1378.4(3)
310	8.5031(4)	8.5128(16)	19.0953(10)	95.510(5)	1375.8(3)
300	8.4989(5)	8.511(2)	19.0749(12)	95.610(6)	1372.9(3)
290	8.4944(4)	8.5090(17)	19.0556(9)	95.688(5)	1370.5(3)
280	8.4921(4)	8.5040(17)	19.0337(9)	95.762(5)	1367.6(3)
270	8.4884(5)	8.500(2)	19.0148(12)	95.853(5)	1364.8(3)
260	8.4870(4)	8.4966(15)	18.9783(8)	95.887(4)	1361.3(2)
250	8.5047(3)	8.5678(13)	18.4505(5)	97.962(3)	1331.5(2)
240	8.4985(3)	8.5600(13)	18.4375(5)	98.026(3)	1328.1(2)
230	8.4942(3)	8.5553(12)	18.4205(5)	98.059(3)	1325.42(19)
220	8.4869(2)	8.5521(11)	18.4052(5)	98.095(3)	1322.56(18)
210	8.4850(2)	8.5454(11)	18.4032(4)	98.123(2)	1320.98(17)
200	8.4796(2)	8.5429(10)	18.3939(4)	98.152(2)	1319.00(17)
190	8.4740(2)	8.5379(10)	18.3859(4)	98.176(2)	1316.72(16)
180	8.4695(2)	8.5310(11)	18.3849(4)	98.215(2)	1314.73(17)
170	8.4661(2)	8.5220(11)	18.3823(5)	98.238(2)	1312.56(18)
160	8.4593(2)	8.5221(10)	18.3689(4)	98.266(2)	1310.48(16)
150	8.4565(2)	8.5156(10)	18.3624(4)	98.273(2)	1308.56(17)
140	8.4521(2)	8.5117(12)	18.3529(5)	98.298(3)	1306.51(19)
130	8.4443(2)	8.5096(13)	18.3539(5)	98.336(3)	1304.9(2)
120	8.4425(2)	8.5063(12)	18.3461(5)	98.346(2)	1303.55(19)
110	8.4379(2)	8.5014(12)	18.3336(5)	98.352(2)	1301.18(18)
100	8.4329(2)	8.4957(11)	18.3299(4)	98.377(2)	1299.20(17)

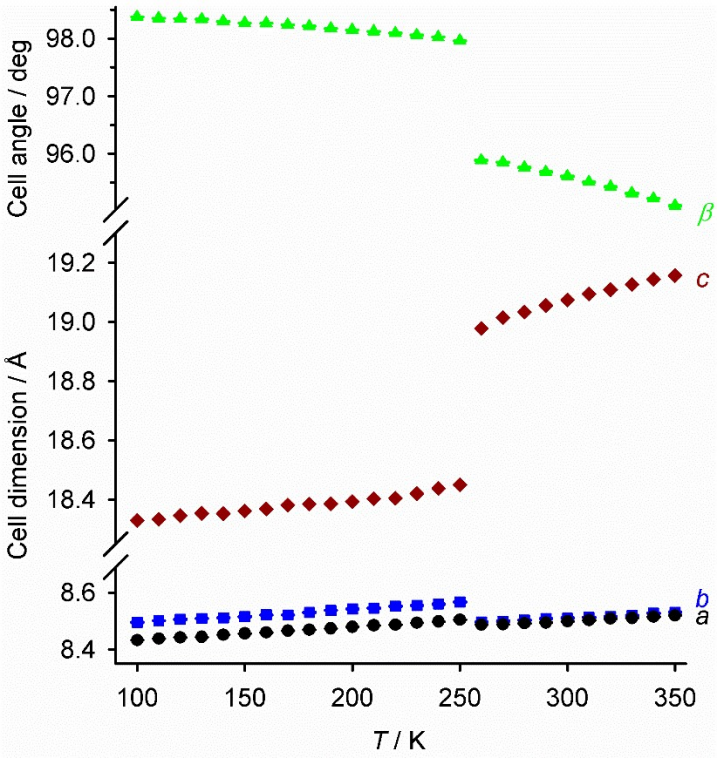

Figure S13 Variable temperature unit cell parameters for $[Fe(bpp)_2][BF_4]_2$ (Table S6). The unit cell volumes are plotted in Figure S21.

Table S7 Variable temperature single crystal unit cells for **1c** (monoclinic, space group $P2_1$).

T / K	a / Å	b / Å	c / Å	β / °	V / Å^3
350	8.501(2)	8.5428(14)	19.105(3)	95.229(16)	1381.8(5)
340	8.4971(16)	8.5339(11)	19.091(3)	95.360(14)	1378.3(4)
330	8.4909(11)	8.5282(11)	19.065(3)	95.482(13)	1374.2(3)
320	8.4829(15)	8.5241(10)	19.048(3)	95.567(13)	1370.9(3)
310	8.4772(16)	8.5161(11)	19.033(3)	95.652(13)	1367.4(4)
300	8.4728(14)	8.5117(10)	19.014(2)	95.734(12)	1364.4(3)
290	8.4738(14)	8.5068(10)	18.989(2)	95.834(12)	1361.7(3)
280	8.4708(13)	8.5033(10)	18.976(2)	95.891(12)	1359.6(3)
270	8.4669(14)	8.5016(9)	18.959(2)	95.965(12)	1357.3(3)
260	8.4648(13)	8.4958(9)	18.948(2)	96.045(11)	1355.5(3)
250	8.4628(13)	8.4945(9)	18.930(2)	96.122(11)	1353.1(3)
240	8.4610(11)	8.4920(8)	18.9078(19)	96.200(10)	1350.6(3)
230	8.4610(11)	8.4896(8)	18.8842(19)	96.304(10)	1348.3(3)
220	8.4609(10)	8.4933(8)	18.8333(18)	96.463(10)	1344.8(3)
210	8.4649(11)	8.5074(8)	18.723(2)	96.839(10)	1338.7(3)
200	8.4600(10)	8.5105(8)	18.6717(18)	97.016(10)	1334.3(2)
190	8.4572(10)	8.5068(8)	18.6360(18)	97.137(10)	1330.4(2)
180	8.4554(10)	8.5030(7)	18.6152(18)	97.221(9)	1327.7(2)
170	8.4532(9)	8.5026(7)	18.6039(16)	97.257(9)	1326.4(2)
160	8.4487(9)	8.4960(7)	18.5898(15)	97.324(8)	1323.5(2)
150	8.4458(9)	8.4915(7)	18.5758(16)	97.369(8)	1321.2(2)
140	8.4452(8)	8.4913(6)	18.5788(15)	97.412(8)	1321.2(2)
130	8.4415(8)	8.4848(6)	18.5610(14)	97.439(8)	1318.22(19)
120	8.4373(8)	8.4791(6)	18.5481(14)	97.487(8)	1315.64(19)
110	8.4350(8)	8.4761(6)	18.5496(14)	97.509(8)	1314.86(19)
100	8.4375(8)	8.4716(6)	18.5416(15)	97.537(8)	1313.89(19)

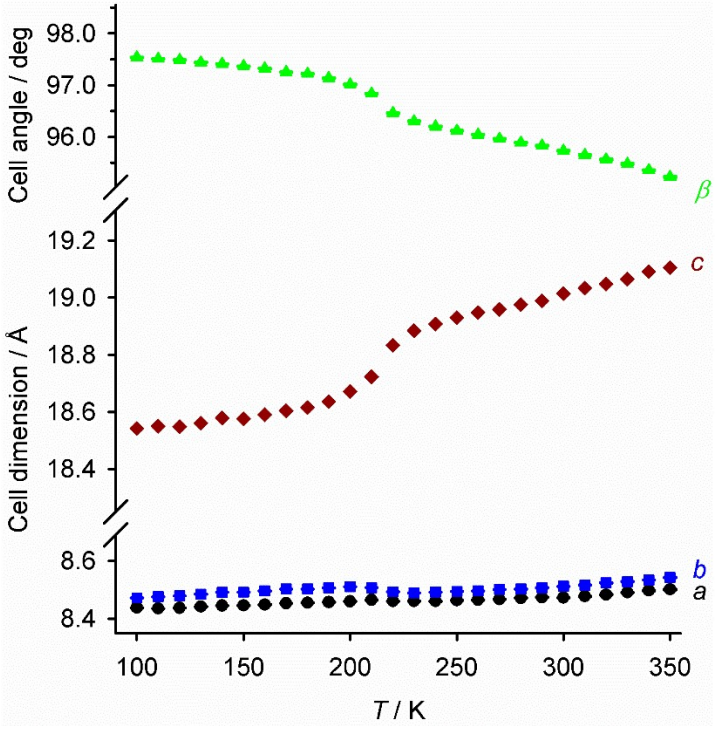

Figure S14 Variable temperature unit cell parameters for **1c** (Table S7). The unit cell volumes are plotted in Figure 7 (main article) and Figure S21.

Table S8 Variable temperature single crystal unit cells for **2c** (monoclinic, space group $P2_1$).

T / K	a / Å	b / Å	c / Å	β / °	V / Å^3
350	8.5517(6)	8.6142(5)	18.8957(17)	95.994(7)	1384.36(18)
340	8.5459(6)	8.6080(5)	18.8764(16)	96.090(7)	1380.76(17)
330	8.5393(6)	8.6027(5)	18.8548(16)	96.182(7)	1377.04(17)
320	8.5342(6)	8.5976(5)	18.8303(15)	96.290(7)	1373.33(16)
310	8.5304(5)	8.5940(5)	18.8108(15)	96.408(7)	1370.42(16)
300	8.5272(5)	8.5908(5)	18.7743(15)	96.521(7)	1366.42(16)
290	8.5220(5)	8.5884(4)	18.7406(14)	96.671(6)	1362.36(15)
280	8.5182(5)	8.5892(4)	18.6907(13)	96.881(6)	1357.65(14)
270	8.5163(5)	8.5908(4)	18.6150(12)	97.174(6)	1351.25(13)
260	8.5098(5)	8.5857(4)	18.5607(11)	97.372(5)	1344.89(13)
250	8.5014(5)	8.5808(4)	18.5344(11)	97.479(5)	1340.57(12)
240	8.4981(4)	8.5761(4)	18.5057(10)	97.543(5)	1337.04(12)
230	8.4875(5)	8.5688(4)	18.4972(11)	97.599(5)	1333.43(12)
220	8.4807(4)	8.5624(4)	18.4814(11)	97.665(5)	1330.05(12)
210	8.4767(4)	8.5566(4)	18.4654(10)	97.686(5)	1327.30(12)
200	8.4734(4)	8.5513(3)	18.4455(9)	97.739(4)	1324.36(11)
190	8.4617(4)	8.5425(4)	18.4454(10)	97.744(5)	1321.16(11)
180	8.4582(4)	8.5394(4)	18.4408(10)	97.774(5)	1319.70(11)
170	8.4546(4)	8.5328(3)	18.4275(9)	97.804(4)	1317.08(10)
160	8.4462(4)	8.5269(3)	18.4196(9)	97.849(4)	1314.15(11)
150	8.4438(4)	8.5229(3)	18.4120(9)	97.844(4)	1312.63(10)
140	8.4428(4)	8.5196(3)	18.4059(9)	97.894(4)	1311.37(10)
130	8.4378(4)	8.5142(3)	18.3947(9)	97.915(4)	1308.89(10)
120	8.4338(4)	8.5097(3)	18.3894(9)	97.948(4)	1307.11(10)
110	8.4289(3)	8.5044(3)	18.3741(8)	97.988(4)	1304.33(9)
100	8.4272(3)	8.5017(3)	18.3748(8)	97.979(4)	1303.71(9)

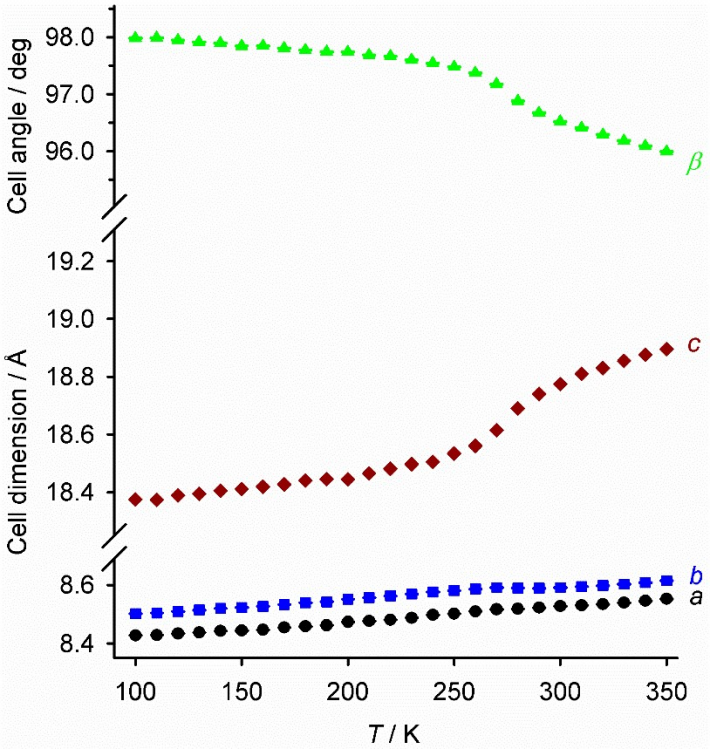

Figure S15 Variable temperature unit cell parameters for **2c** (Table S8). The unit cell volumes are plotted in Figure 7 (main article) and Figure S21.

Table S9 Variable temperature single crystal unit cells for **3c** (monoclinic, space group $P2_1$).

T / K	a / Å	b / Å	c / Å	β / °	V / Å^3
350	8.5444(8)	8.5967(9)	19.003(2)	95.778(9)	1388.8(2)
340	8.5359(7)	8.5886(8)	18.9753(18)	95.889(8)	1383.8(2)
330	8.5310(7)	8.5843(8)	18.9666(18)	95.967(8)	1381.4(2)
320	8.5251(6)	8.5760(7)	18.9434(18)	96.073(8)	1377.2(2)
310	8.5223(7)	8.5757(7)	18.9274(18)	96.169(8)	1375.3(2)
300	8.5172(6)	8.5691(7)	18.9034(17)	96.245(8)	1371.5(2)
290	8.5123(6)	8.5659(7)	18.8801(16)	96.359(7)	1368.19(18)
280	8.5093(6)	8.5609(7)	18.8535(15)	96.449(7)	1364.73(18)
270	8.4995(6)	8.5535(7)	18.7977(16)	96.588(7)	1357.57(18)
260	8.4985(6)	8.5608(7)	18.7258(16)	96.850(7)	1352.64(18)
250	8.4906(5)	8.5593(6)	18.6165(14)	97.185(7)	1342.29(17)
240	8.4865(5)	8.5586(6)	18.5666(13)	97.367(6)	1337.40(15)
230	8.4818(5)	8.5533(6)	18.5438(12)	97.462(6)	1333.91(15)
220	8.4787(5)	8.5510(5)	18.5283(12)	97.534(6)	1331.74(14)
210	8.4751(5)	8.5469(5)	18.5142(11)	97.602(5)	1329.29(13)
200	8.4712(4)	8.5419(5)	18.5042(11)	97.631(5)	1327.11(13)
190	8.4636(4)	8.5322(5)	18.4815(11)	97.691(5)	1322.59(13)
180	8.4591(4)	8.5254(5)	18.4722(10)	97.694(5)	1320.17(12)
170	8.4578(4)	8.5232(5)	18.4716(11)	97.703(5)	1319.56(12)
160	8.4527(4)	8.5153(4)	18.4516(9)	97.748(5)	1315.96(11)
150	8.4489(4)	8.5098(4)	18.4427(9)	97.770(5)	1313.83(11)
140	8.4450(4)	8.5043(4)	18.4350(9)	97.776(5)	1311.80(11)
130	8.4424(4)	8.4985(4)	18.4313(9)	97.801(5)	1310.16(11)
120	8.4399(4)	8.4987(4)	18.4180(9)	97.900(5)	1308.55(11)
110	8.4360(4)	8.4937(4)	18.4123(10)	97.911(5)	1306.74(11)
100	8.4335(4)	8.4893(4)	18.4065(10)	97.937(5)	1305.18(11)

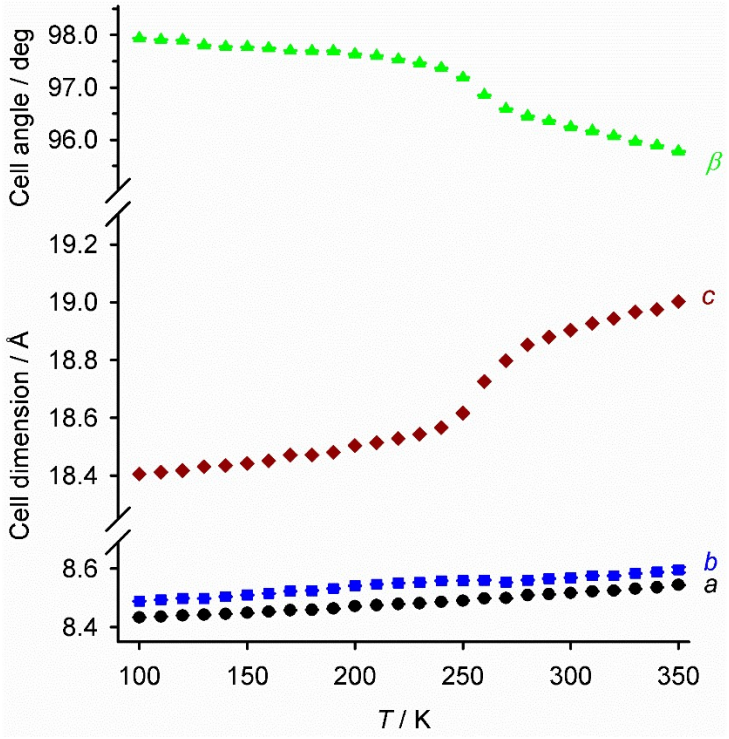

Figure S16 Variable temperature unit cell parameters for **3c** (Table S9). The unit cell volumes are plotted in Figure 7 (main article) and Figure S21.

Table S10 Variable temperature single crystal unit cells for $[Zn(bpp)_2][BF_4]_2$ (monoclinic, space group $P2_1$).

T / K	a / Å	b / Å	c / Å	β / °	V / Å^3
350	8.5273(11)	8.5745(10)	19.121(2)	95.388(11)	1391.9(3)
340	8.5219(11)	8.5705(11)	19.104(2)	95.497(11)	1388.9(3)
330	8.5180(11)	8.5637(10)	19.088(2)	95.595(11)	1385.7(3)
320	8.5148(11)	8.5546(10)	19.070(2)	95.695(11)	1382.2(3)
310	8.5050(9)	8.5528(9)	19.0504(19)	95.771(10)	1378.7(3)
300	8.4933(10)	8.5373(9)	19.016(2)	95.875(10)	1371.6(3)
290	8.4850(8)	8.5311(8)	18.9957(18)	95.956(9)	1367.6(2)
280	8.4789(9)	8.5266(9)	18.9739(19)	96.028(10)	1364.2(2)
270	8.4810(9)	8.5261(9)	18.9718(19)	96.104(10)	1364.1(2)
260	8.4708(8)	8.5161(7)	18.9457(16)	96.148(9)	1358.8(2)
250	8.4716(8)	8.5137(8)	18.9376(16)	96.206(9)	1357.9(2)
240	8.4701(7)	8.5085(7)	18.9173(15)	96.317(8)	1355.0(2)
230	8.4629(7)	8.5032(6)	18.8989(14)	96.340(7)	1351.68(18)
220	8.4591(7)	8.4986(6)	18.8844(13)	96.399(7)	1349.15(17)
210	8.4578(7)	8.4943(6)	18.8658(13)	96.466(7)	1346.75(17)
200	8.4569(6)	8.4863(6)	18.8610(12)	96.583(7)	1344.69(16)
190	8.4572(7)	8.4787(7)	18.8501(14)	96.695(8)	1342.46(19)
180	8.4483(6)	8.4758(6)	18.8273(12)	96.657(7)	1339.06(16)
170	8.4498(6)	8.4705(6)	18.8292(12)	96.767(7)	1338.30(16)
160	8.4480(6)	8.4687(6)	18.8177(12)	96.789(7)	1336.85(16)
150	8.4452(6)	8.4640(5)	18.8016(12)	96.803(6)	1334.47(15)
140	8.4400(6)	8.4570(5)	18.7831(11)	96.834(6)	1331.15(14)
130	8.4408(6)	8.4524(5)	18.7806(11)	96.924(6)	1330.12(15)
120	8.4401(5)	8.4514(5)	18.7766(10)	96.947(6)	1329.52(13)
110	8.4379(5)	8.4463(5)	18.7598(10)	96.953(5)	1327.16(13)
100	8.4358(5)	8.4419(5)	18.7493(10)	96.984(5)	1325.30(13)

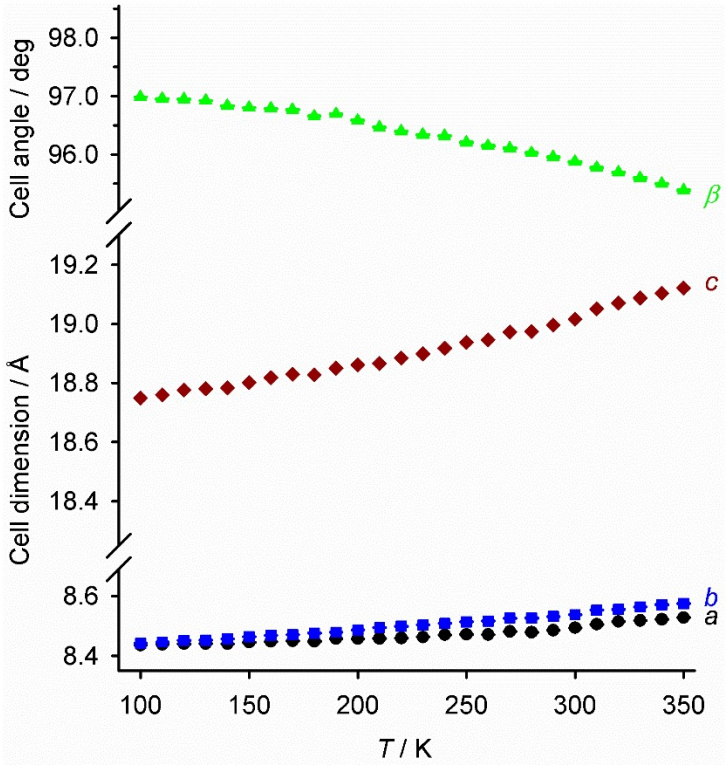

Figure S17 Variable temperature unit cell parameters for $[Zn(bpp)_2][BF_4]_2$ (Table S10). The unit cell volumes are plotted in Figure S22.

Table S11 Variable temperature single crystal unit cells for $[Ru(bpp)_2][BF_4]_2$ (monoclinic, space group $P2_1$).

T / K	a / Å	b / Å	c / Å	β / °	V / Å^3
350	8.5450(5)	8.6258(6)	18.6681(14)	96.824(6)	1366.22(16)
340	8.5366(5)	8.6166(5)	18.6562(13)	96.882(6)	1362.39(15)
330	8.5292(5)	8.6090(5)	18.6354(13)	96.952(6)	1358.29(15)
320	8.5248(5)	8.6038(5)	18.6179(12)	97.001(5)	1355.35(14)
310	8.5190(5)	8.5989(5)	18.6003(12)	97.060(5)	1352.22(14)
300	8.5157(5)	8.5940(5)	18.5956(11)	97.108(5)	1350.43(14)
290	8.5085(5)	8.5870(5)	18.5804(11)	97.160(5)	1346.95(14)
280	8.5053(5)	8.5837(5)	18.5727(11)	97.210(5)	1345.21(13)
270	8.5000(5)	8.5779(5)	18.5543(11)	97.243(5)	1342.04(13)
260	8.4976(5)	8.5740(5)	18.5443(10)	97.287(5)	1340.19(13)
250	8.4914(5)	8.5692(5)	18.5287(11)	97.325(5)	1337.22(13)
240	8.4884(5)	8.5664(5)	18.5166(10)	97.374(5)	1335.30(13)
230	8.4863(5)	8.5629(5)	18.5037(10)	97.399(5)	1333.42(13)
220	8.4824(4)	8.5580(5)	18.4968(10)	97.442(5)	1331.42(12)
210	8.4752(5)	8.5500(5)	18.4868(10)	97.476(5)	1328.22(12)
200	8.4728(5)	8.5455(5)	18.4842(10)	97.521(5)	1326.82(12)
190	8.4683(5)	8.5411(5)	18.4545(9)	97.545(5)	1323.24(12)
180	8.4639(5)	8.5351(4)	18.4498(9)	97.572(5)	1321.21(12)
170	8.4600(4)	8.5307(4)	18.4397(9)	97.605(4)	1319.07(12)
160	8.4552(4)	8.5242(4)	18.4265(9)	97.630(4)	1316.31(12)
150	8.4548(4)	8.5220(4)	18.4176(9)	97.660(5)	1315.19(12)
140	8.4499(4)	8.5162(4)	18.4153(9)	97.688(4)	1313.26(11)
130	8.4465(5)	8.5105(4)	18.4239(9)	97.717(5)	1312.38(12)
120	8.4433(4)	8.5068(4)	18.3991(9)	97.742(4)	1309.47(11)
110	8.4409(4)	8.5032(4)	18.3900(9)	97.761(4)	1307.87(11)
100	8.4381(4)	8.4989(4)	18.3902(8)	97.808(4)	1306.62(11)

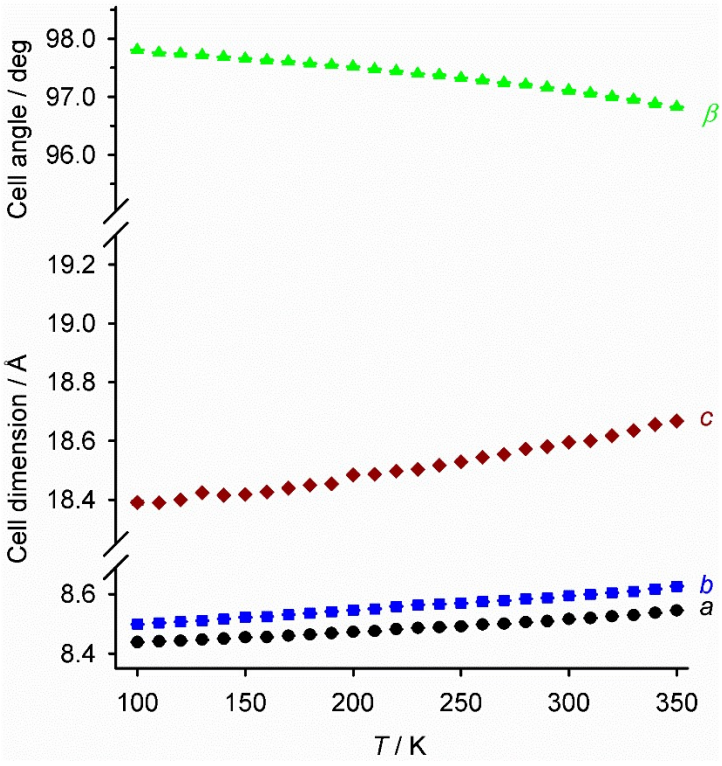

Figure S18 Variable temperature unit cell parameters for $[Ru(bpp)_2][BF_4]_2$ (Table S11). The unit cell volumes are plotted in Figure S22.

Table S12 Variable temperature single crystal unit cells for $[Ni(bpp)_2][BF_4]_2$ (monoclinic, space group $P2_1$).

T / K	a / Å	b / Å	c / Å	β / °	V / Å^3
350	8.5233(8)	8.6038(7)	18.8098(16)	96.240(8)	1371.2(2)
340	8.5345(7)	8.6100(6)	18.8221(14)	96.378(7)	1374.52(18)
330	8.5172(7)	8.5998(6)	18.7982(14)	96.421(7)	1368.27(18)
320	8.5167(6)	8.5975(6)	18.7852(13)	96.490(7)	1366.69(17)
310	8.5116(6)	8.5916(6)	18.7702(13)	96.569(6)	1363.62(16)
300	8.5098(8)	8.5811(9)	18.747(2)	96.615(9)	1359.9(2)
290	8.5030(6)	8.5842(6)	18.7385(12)	96.660(6)	1358.51(16)
280	8.4960(5)	8.5768(5)	18.7254(11)	96.733(6)	1355.07(14)
270	8.4922(5)	8.5729(5)	18.7121(10)	96.796(5)	1352.73(13)
260	8.4885(5)	8.5680(5)	18.6991(10)	96.837(5)	1350.31(13)
250	8.4866(5)	8.5642(5)	18.6893(10)	96.891(5)	1348.53(14)
240	8.4817(5)	8.5626(4)	18.6720(9)	96.930(5)	1346.16(12)
230	8.4806(5)	8.5552(4)	18.6656(9)	96.985(5)	1344.19(12)
220	8.4771(5)	8.5501(5)	18.6612(11)	97.082(6)	1342.26(14)
210	8.4748(4)	8.5457(4)	18.6401(8)	97.087(4)	1339.67(11)
200	8.4706(4)	8.5420(4)	18.6330(8)	97.119(4)	1337.82(11)
190	8.4671(4)	8.5375(4)	18.6199(8)	97.153(4)	1335.53(10)
180	8.4614(4)	8.5324(4)	18.6083(8)	97.165(4)	1332.96(10)
170	8.4585(4)	8.5293(3)	18.6005(8)	97.210(4)	1331.33(10)
160	8.4575(4)	8.5233(3)	18.5865(8)	97.258(4)	1329.09(10)
150	8.4566(4)	8.5197(4)	18.5807(8)	97.259(4)	1327.97(10)
140	8.4525(4)	8.5159(3)	18.5743(7)	97.332(4)	1326.07(9)
130	8.4485(3)	8.5110(3)	18.5649(7)	97.349(4)	1323.95(9)
120	8.4443(4)	8.5074(3)	18.5579(8)	97.378(4)	1322.14(10)
110	8.4451(3)	8.5033(3)	18.5529(7)	97.422(4)	1321.14(9)
100	8.4441(3)	8.4984(3)	18.5430(7)	97.455(4)	1319.41(9)

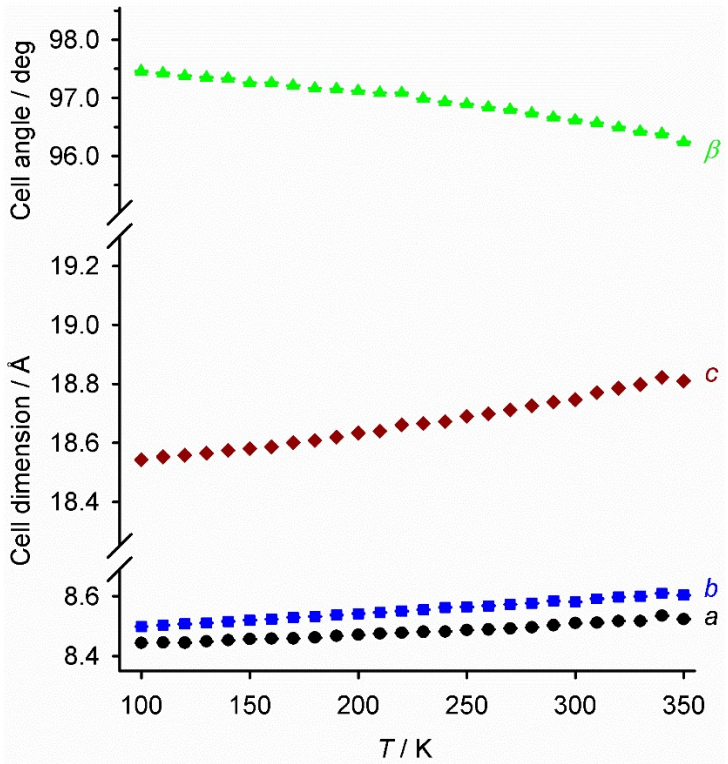

Figure S19 Variable temperature unit cell parameters for $[Ni(bpp)_2][BF_4]_2$ (Table S12). The unit cell volumes are plotted in Figure S22.

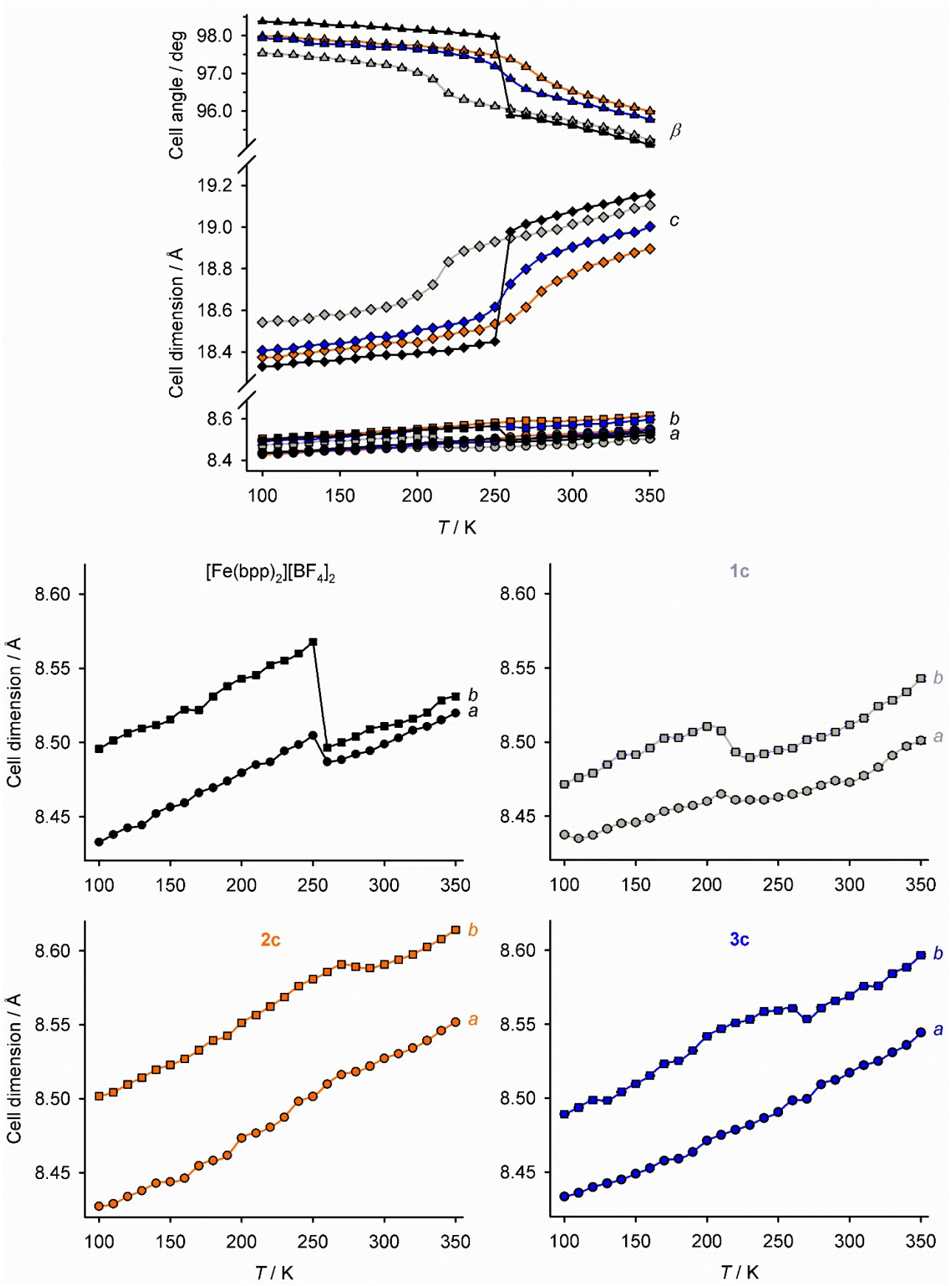

Figure S20 Comparison of the temperature-dependent unit cells of $[Fe(bpp)_2][BF_4]_2$ (black), **1c** (grey), **2c** (orange) and **3c** (blue). Top: all the unit cell dimensions on one plot. Bottom: expansion of the cation layer dimensions *a* and *b*, plotted separately for each compound.

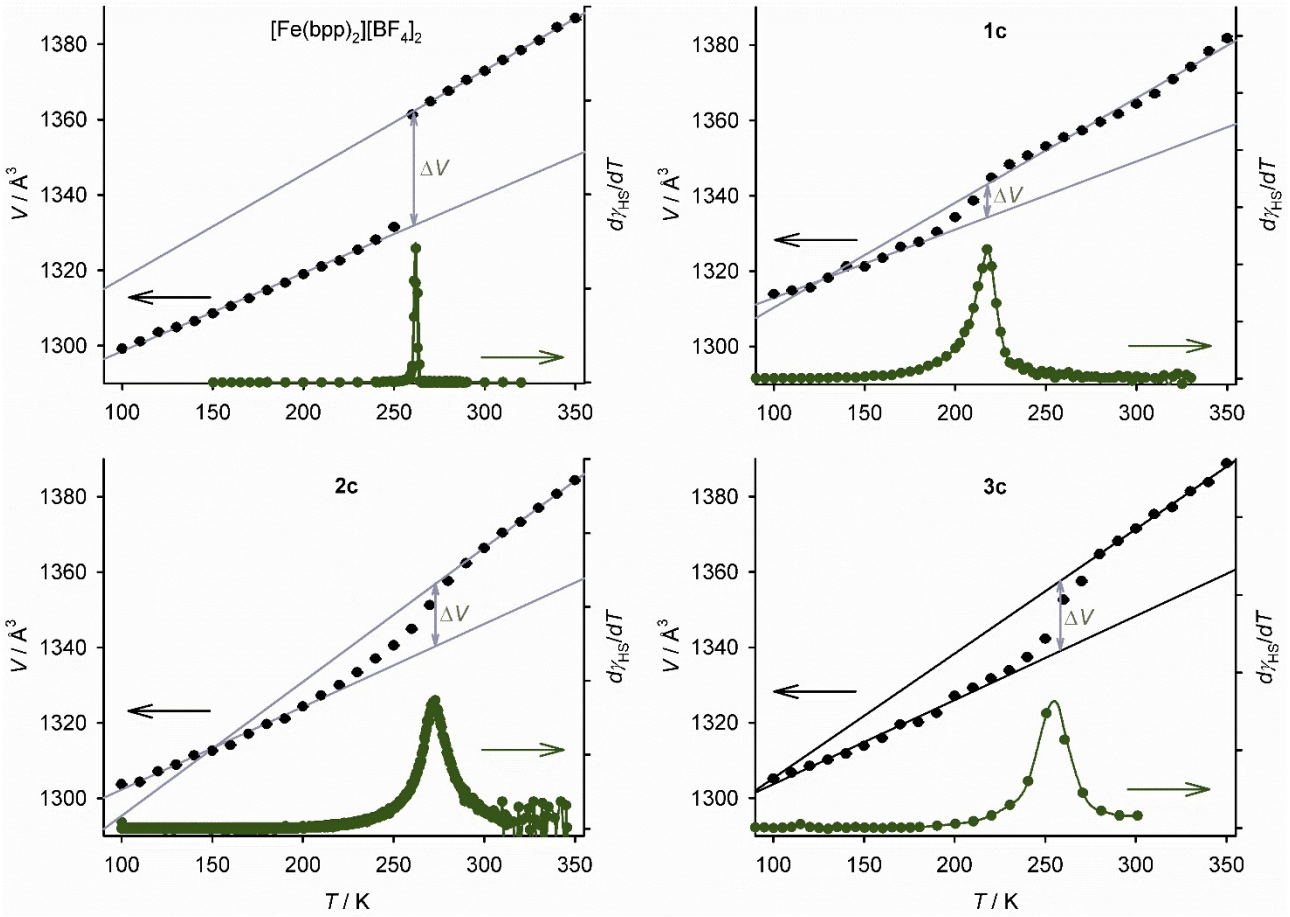

Figure S21 Variable temperature unit cell volumes for $[Fe(bpp)_2][BF_4]_2$ and the solid solutions **1c**-**3c** (Tables S6-S9). The lines showing the thermal expansion linear regression fits for the high-spin and low-spin forms of each compound, with the volume change at $T_{½}$ indicated in grey. The first derivative of the magnetic susceptibility data for each compound is also shown, as green data points connected by a spline curve.

Magnetic data for $[Fe(bpp)_2][BF_4]_2$ and **3c** are taken from ref. 11.

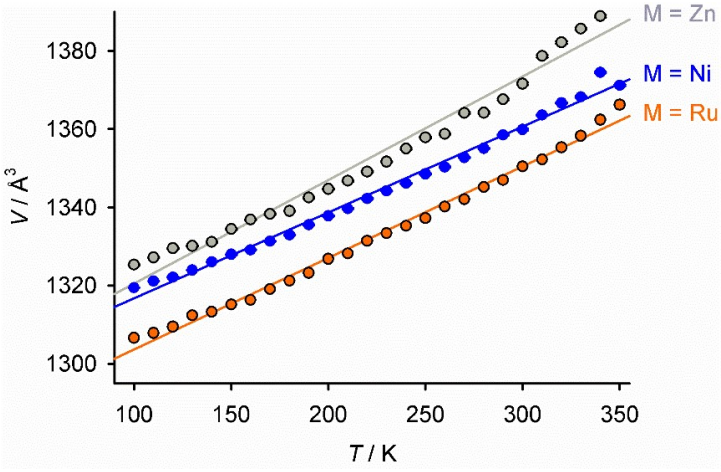

Figure S22 Variable temperature unit cell volumes for the pure dopant compounds $[M(bpp)_2][BF_4]_2$ (Tables S10-S12), showing the linear regression fits used to calculate α_V.

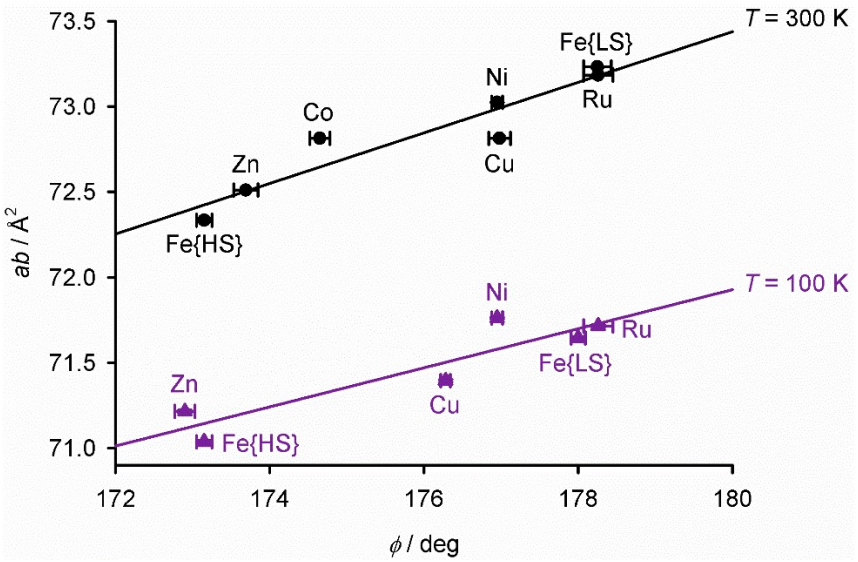

Figure S23 The relationship between the *trans*-N{pyridyl}–M–N{pyridyl} angle (ϕ, page S11) and the area of the terpyridine embrace cation layers (the product of the *a* and *b* unit cell dimensions) in the metal-pure $[M(bpp)_2][BF_4]_2$ crystals. The graph includes literature data for M = Co[23] and Cu,[9] which are isomorphous with the compounds in this work.

Unit cell data at two temperatures are plotted. Distinct ϕ values at, or near, each temperature are also included where these are available (M = Fe{LS}, Cu and Zn). Crystal structures for M = Ni and Ru are only available at one temperature, while the crystal structure of M = Fe{HS} near 100 K cannot be measured.

This graph, and Figure 8 in the main article, show the dimensions of the cation layers (Figure S11) mostly reflect the angular coordination geometry of the metal ion, as exemplified by ϕ. That is, $[M(bpp)_2]^{2+}$ molecules whose structures approach ideal D_{2d} symmetry (ϕ = 180°) pack less densely in two dimensions. The M–N bond lengths have a smaller effect on the packing geometry, but may account for some of the scatter in the Figure.

Table S13 Anisotropic thermal expansion coefficients for the compounds in this work. The α_V{100 K} and α_{TE}{100 K} values are taken from Table 5 (main article). The α_{TE} parameter is the 2D thermal expansion coefficient of the terpyridine embrace cation layers (Figure S11).[a]

	Temperature range / K	α_i / 10^6 K^{-1}	Direction			Cartesian vector
			a	***b***	***c***	
$[Fe(bpp)_2][BF_4]_2$, high-spin	270-350					
α_V{300 K}		201(2)	–	–	–	–
α_V{100 K}		209(2)	–	–	–	–
α_1{100 K}		–6(2)	–0.951	0	0.309	[$\bar{3}$01]
α_2{100 K}		44(2)	0	1	0	[010]
α_3{100 K}		167.0(10)	0.866	0	0.500	[503]
α_{TE}{100 K}		38(3)	–	–	–	–
$[Fe(bpp)_2][BF_4]_2$, low-spin	100-250					
α_V{300 K}		155(4)	–	–	–	–
α_V{100 K}		160(4)	–	–	–	–
α_1{100 K}		26.7(10)	–0.787	0	0.617	[$\bar{5}$04]
α_2{100 K}		55.3(11)	0	1	0	[010]
α_3{100 K}		76(2)	0.955	0	0.297	[301]
α_{TE}{100 K}		82.0(15)	–	–	–	–
1c, high-spin	240-350					
α_V{300 K}		204(8)	–	–	–	–
α_V{100 K}		213(8)	–	–	–	–
α_1{100 K}		–4(2)	–0.956	0	0.295	[$\bar{3}$01]
α_2{100 K}		54(3)	0	1	0	[010]
α_3{100 K}		158(4)	0.857	0	0.516	[503]
α_{TE}{100 K}		50(4)	–	–	–	–
1c, low-spin	100-180					
α_V{300 K}		134(7)	–	–	–	–
α_V{100 K}		140(7)	–	–	–	–
α_1{100 K}		8(2)	0.959	0	–0.311	[$\bar{3}$01]
α_2{100 K}		49(2)	0	1	0	[010]
α_3{100 K}		80(4)	0.863	0	0.505	[503]
α_{TE}{100 K}		57(3)	–	–	–	–
2c, high-spin	300-350					
α_V{300 K}		260(2)	–	–	–	–
α_V{100 K}		273(2)	–	–	–	–
α_1{100 K}		5(2)	–0.960	0	0.294	[$\bar{3}$01]
α_2{100 K}		55(3)	0	1	0	[010]
α_3{100 K}		208(6)	0.851	0	0.526	[503]
α_{TE}{100 K}		60(4)	–	–	–	–
2c, low-spin	100-220					
α_V{300 K}		163(5)	–	–	–	–
α_V{100 K}		170(5)	–	–	–	–
α_1{100 K}		29.4(16)	–0.922	0	0.386	[$\bar{5}$02]
α_2{100 K}		60.1(16)	0	1	0	[010]
α_3{100 K}		78(2)	0.898	0	0.441	[201]
α_{TE}{100 K}		90(2)	–	–	–	–

[a] $\alpha_{TE} = \alpha_1 + \alpha_2$

Table S13 continued

	Temperature range / K	α_i / 10^6 K^{-1}	Direction			Cartesian vector
			a	***b***	***c***	
3c, high-spin	290-350					
α_V{300 K}		241(8)	–	–	–	–
α_V{100 K}		251(8)	–	–	–	–
α_1{100 K}		5(2)	–0.947	0	0.320	[$\bar{3}$01]
α_2{100 K}		59(3)	0	1	0	[010]
α_3{100 K}		182(4)	0.870	0	0.493	[503]
α_{TE}{100 K}		64(4)	–	–	–	–
3c, low-spin	100-220					
α_V{300 K}		165(6)	–	–	–	–
α_V{100 K}		173(6)	–	–	–	–
α_1{100 K}		26(2)	0.917	0	–0.397	[$\bar{5}$02]
α_2{100 K}		62(2)	0	1	0	[010]
α_3{100 K}		81(3)	0.902	0	0.432	[201]
α_{TE}{100 K}		88(3)	–	–	–	–
$[Zn(bpp)_2][BF_4]_2$	100-350					
α_V{300 K}		193(7)	–	–	–	–
α_V{100 K}		204(7)	–	–	–	–
α_1{100 K}		7.0(12)	–0.962	0	0.274	[$\bar{3}$01]
α_2{100 K}		62.9(15)	0	1	0	[010]
α_3{100 K}		127(5)	0.841	0	0.540	[503]
α_{TE}{100 K}		70(2)	–	–	–	–
$[Ni(bpp)_2][BF_4]_2$	100-350					
α_V{300 K}		161(4)	–	–	–	–
α_V{100 K}		168(4)	–	–	–	–
α_1{100 K}		14.2(14)	0.948	0	–0.317	[$\bar{3}$01]
α_2{100 K}		52.1(8)	0	1	0	[010]
α_3{100 K}		98(3)	0.866	0	0.500	[503]
α_{TE}{100 K}		66.3(16)	–	–	–	–
$[Ru(bpp)_2][BF_4]_2$	100-350					
α_V{300 K}		173(4)	–	–	–	–
α_V{100 K}		180(4)	–	–	–	–
α_1{100 K}		25.3(6)	0.923	0	–0.386	[$\bar{5}$02]
α_2{100 K}		57.8(8)	0	1	0	[010]
α_3{100 K}		93(3)	0.897	0	0.442	[201]
α_{TE}{100 K}		83.1(10)	–	–	–	–

[a] $\alpha_{TE} = \alpha_1 + \alpha_2$

All the parameters at 100 K were calculated using the *PASCal* web resource.[26] *PASCal* scales its results to the lowest temperature in the input data, which is 100 K in most cases. Unit cell parameters from the high-spin forms of the iron-containing samples were extrapolated to 100 K for the *PASCal* calculation, to give self-consistent results.

The α_V values calculated by this method are consistently 4-6 % larger at 100 K than at 300 K, which simply reflects the smaller V_0 reference volume used in the low temperature calculation.

Discussion of Table S13.

The principal component vectors of thermal expansion from the *PASCal* outputs are cartesian vectors, *not* unit cell vectors, which are listed in order of increasing magnitude.[26] In monoclinic symmetry one α_i vector must lie parallel to *b*, which is α_2 in this system. The other two α_i vectors can take any orientation in the (010) crystal plane. Inspection shows that both α_1 and α_2 lie within the terpyridine embrace cation layers, while α_3 is approximately perpendicular to those layers (Figure 6, main article).

Cations related by translation along *a* and *b* are in close contact with each other, through edge-to-face C–H$\cdots\pi$ and face-to-face $\pi\cdots\pi$ contacts between their pyrazolyl rings (Figure S11). This leads to interdigitated layers of cations in the (001) plane. The two smallest expansion components α_1 and α_2 lie within the cation layers, showing these are the stiffest dimensions of the crystal.

The 2D thermal expansiveness of the cation layers (α_{TE}) is the sum of $\alpha_1 + \alpha_2$. In most cases, the low-spin iron-containing crystals give higher values for this parameter than their high-spin forms. That is, the cation layers in the low-spin iron crystals are *more* deformable in the low-spin state. The cation layers in the low-spin d^6 precursor crystal $[Ru(bpp)_2][BF_4]_2$ are similarly soft.

The exception to that generalisation is **1c**, whose high-spin and low-spin cation layers have identical α_{TE} values within experimental error. This is discussed further in the main article.

The largest expansion vector, α_3, shows the most deformable direction in the crystal. This corresponds to compression or tension perpendicular to the cation layers, where the intermolecular interactions in the crystal are weakest (Figure 6, main article). α_3 is always 2-3x larger in the high-spin states of the iron-containing crystals.

The large decrease in α_3 during high→low-spin SCO explains why α_V is always smaller in the low-spin state.

Table S14 $\alpha_V\{100\ K\}$ thermal expansion coefficients in isomorphous high-spin and low-spin states of literature iron(II) SCO complexes, whose unit cell data have been tabulated at multiple temperatures. All the values are scaled against the unit cell volume (V) at 100 K, which was derived by linear extrapolation of the experimental data if required. Values in square brackets are from the isomorphous zinc(II) analogues of those complexes, fitted over a similar temperature range. $\Delta V_{SCO}\{T\}$ is the isothermal difference in the unit cell volumes of the spin states of the crystal, at temperature T.

	High-spin		Low-spin			
	Temperature range / K	$\alpha_V\{100\ K\}$ / $10^6\ K^{-1}$	Temperature range / K	$\alpha_V\{100\ K\}$ / $10^6\ K^{-1}$	$\Delta V_{SCO}\{T\}$ / Å^3	Ref.
$[Fe(pic)_3]Cl_2 \cdot EtOH$	125-298	228(4)	50-100	168(15)[b]	64 {10 K}	27, 28
$[Fe(mtz)_6][BF_4]_2$	90-290	242(2) [227(2)]	<50	–	55(2) {10 K}	29
$[Fe(ptz)_6][BF_4]_2$	140-300	342(6) [279(7)]	50-100	154(9)[b,c]	65(2) {10 K}	30
$[Fe(\{MePy\}_3tren)][ClO_4]_2$	290-330	301(5) [255(1)]	80-170	114(7)	–	31
$[Fe(NCS)_2(abpt)_2]$, polymorph D	225-300	127.4(9)	30-100	67(7)	59.2(2) {30 K}	32
$[Fe(5\text{-}\{NO_2\}_2\text{-saltrien})]$	220-300	109(3)	90-130	77(6)	–	33
$[Fe(bpp^{S\textit{i}Pr})_2][BF_4]_2 \cdot MeCN$[d]	165-230	222.8(5)	120-165	140(2)	–7.4(16) {85 K}[e]	34, 35
$[Fe(bpp^{S\textit{i}Pr})_2][BF_4]_2 \cdot MeNO_2$[d]	180-230	236(3)	120-150	161(6)	–	35

[a]abpt = 4-amino-3,5-bis(pyridin-2-yl)-1,2,4-triazole; $bpp^{S\textit{i}Pr}$ = 4-(*iso*propylsulfanyl)-2,6-di(pyrazol-1-yl)pyridine; $\{MePy\}_3tren$ = *tris*[3-aza-4-(6-methyl-2-pyridyl)-but-3-enyl]amine; mtz = 5-methyltetrazole; $H_2[5\text{-}\{NO_2\}_2\text{-saltrien}]$ = 5-nitrosalicylaldehyde-1,4,7,10-tetraazadecane; pic = 2-(aminomethyl)pyridine; ptz = 5-{*n*-propyl}tetrazole. [b]Data at T <50 K were omitted from these linear regression fits, to avoid contamination by non-linear dV/dT behaviour at very low temperatures (Figure S24). [c]Data are for the supercooled low-spin form of this material, which is isomorphous with the high-spin phase. [d]These two crystals are isomorphous. [e]This compound undergoes a negative volume change during the LS→HS transition by photocrystallography.

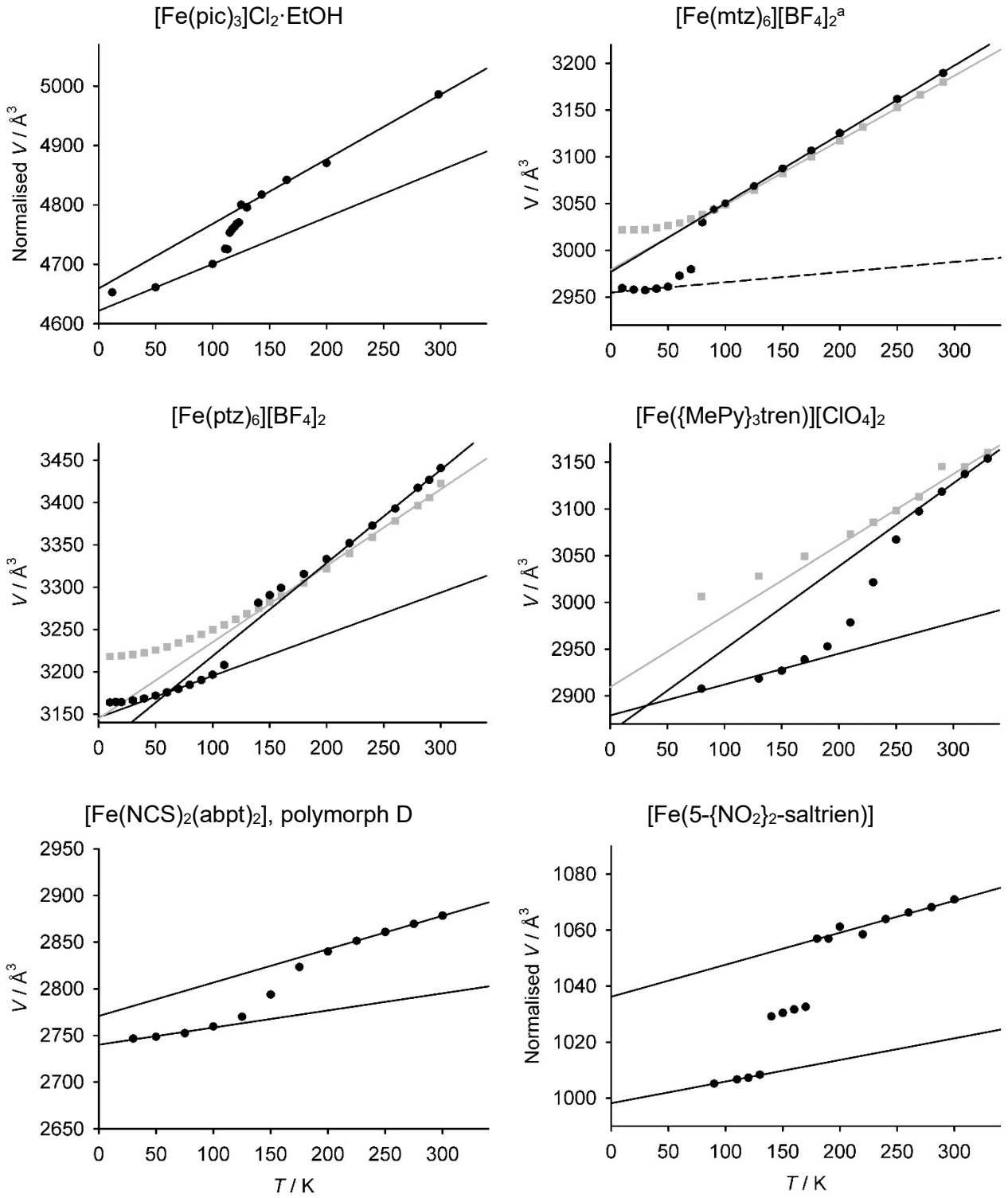

Figure S24 Variable temperature unit cell data for the compounds in Table S14, showing the regression lines used to calculate their thermal expansion coefficients. The grey data are from the corresponding isomorphous zinc(II) complexes. Data at $T < 50$ K are not included in the linear regression fits.

The graphs labelled 'normalised *V*' include data from an intermediate re-entrant mixed-spin phase involved in the spin-transition process. Each graph is plotted over the same temperature range and with vertical axis ranges scaled proportionately with the magnitude of the cell volumes, so the slopes of their regression lines are visually comparable.

[a]A meaningful α_V{low-spin} value for $[Fe(mtz)_6][BF_4]_2$ cannot be measured (dashed line), because its unit cell dimensions have plateaued in its low-spin temperature range $T < 50$ K. The same low-temperature behaviour is shown by the isomorphous zinc complex, and by $[M(ptz)_6][BF_4]_2$ (M = Fe, Zn).

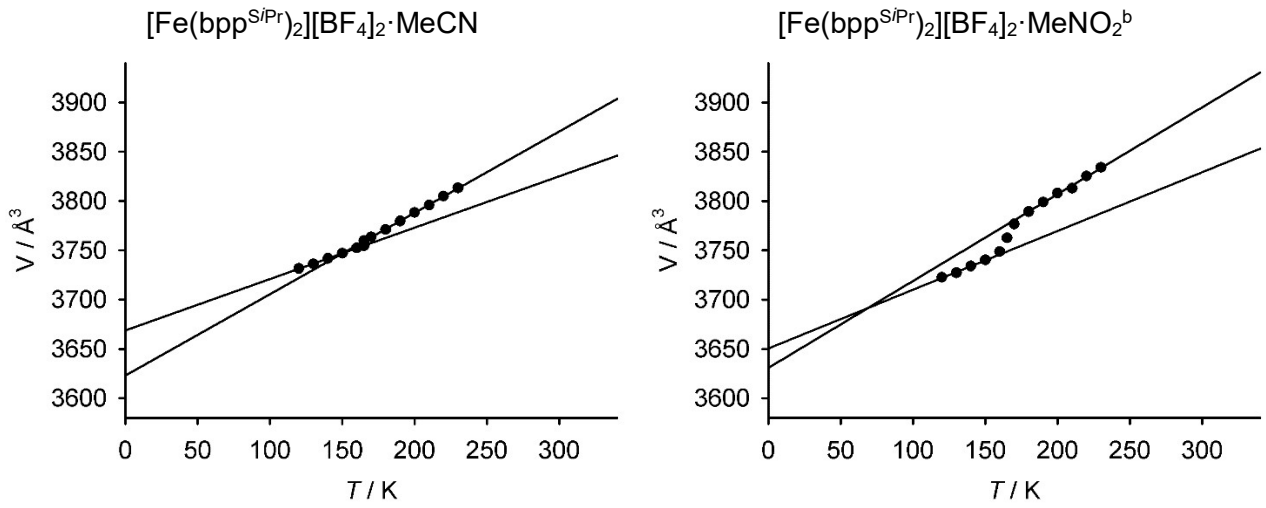

Figure S24 continued.

[b]This crystal undergoes a low-temperature phase transition below 80 K, to a low temperature phase with a tripled unit cell volume.[34] Hence the predicted negative ΔV {$T < 80$ K} for this crystal at low temperature does not occur in practise. A negative ΔV {85 K} does occur experimentally for the acetonitrile solvate, however.[35]

Discussion of the data in Table S14.

The wide distribution of errors in the Table reflects the different number of datapoints in each calculation, and the linearity of the *V vs. T* data in the high-spin and low-spin temperature ranges.

Three trends can be observed from the Table:

(i) Isothermal α_V for the high-spin state is consistently 1.3-2.5x larger than for the low-spin state.

(ii) α_V for the zinc complexes is 82-94 % as large as for the corresponding high-spin iron(II) crystal.

(iii) The neutral complexes give smaller α_V values than the complex salts. Although the sample is small, each spin state of the charge-neutral materials shows less variation than in the salt crystals.

Points (i) and (ii) are also consistent with the $[M(bpp)_2][BF_4]_2$ (M = Fe, Zn) data tabulated in the main article.

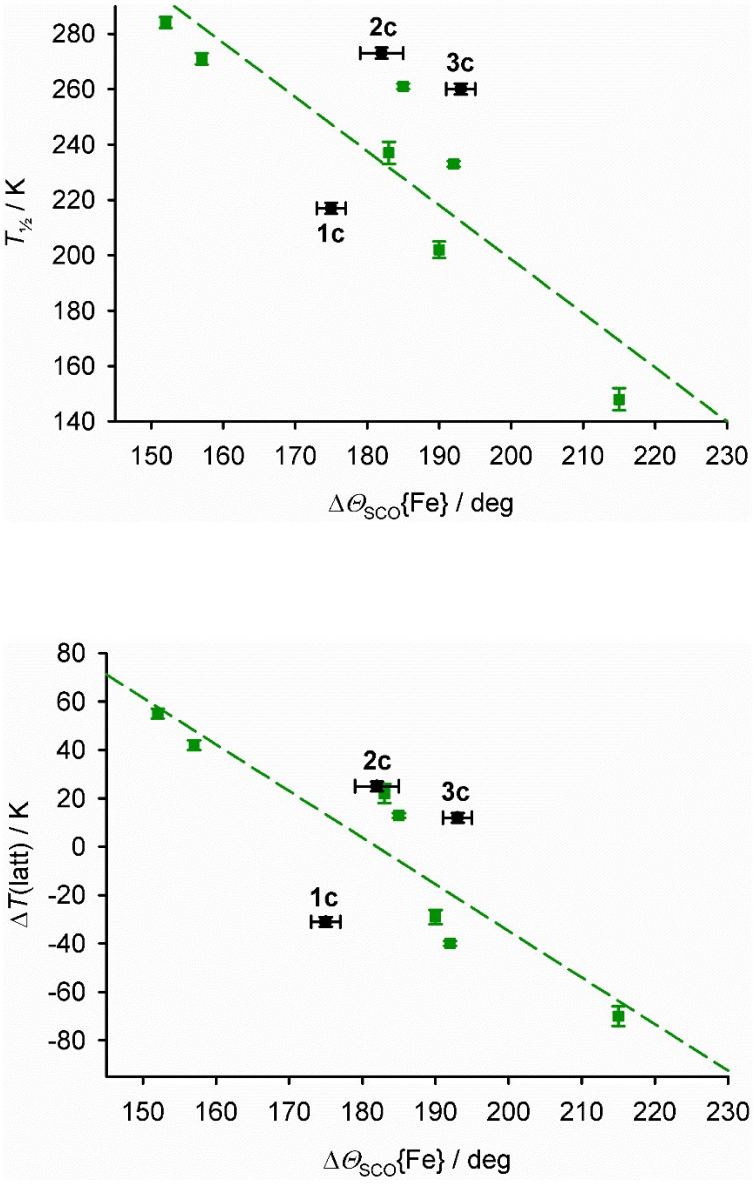

Figure S25 The relationship between $\Delta\Theta_{SCO}\{Fe\}$ and the SCO temperature, expressed as $T_{½}$ (top) and ΔT(latt) (bottom), for salts of $[Fe(bpp)_2]^{2+}$ derivatives with terpyridine embrace crystal packing. The green data points and line show the published correlation,[20] while **1c**-**3c** are plotted in black. The ΔT(latt) plot is the same as in Figure 9 of the main article.

While the placement of **1c**-**3c** is similar in the two plots, the base correlation in the top graph is more scattered. That's because the green data points contain a number of molecules with different patterns of ligand substituents, which also affect $T_{½}$ by change the molecular ligand field. The ΔT(latt) corrects for ligand field effects, so the contribution to the SCO temperature can be quantified in isomorphous crystals of different molecules.[20]

References

1. C. Baldé, C. Desplanches, J.-F. Létard and G. Chastanet, *Polyhedron*, 2017, **123**, 138–144.
2. C. Baldé, C. Desplanches, P. Gütlich, E. Freysz and J.-F. Létard, *Inorg. Chim. Acta*, 2008, **361**, 3529–3533.
3. C. Baldé, C. Desplanches, F. Le Gac, P. Guionneau and J.-F. Létard, *Dalton Trans.*, 2014, **43**, 7820–7829.
4. a) J.-P. Martin, J. Zarembowitch, A. Dworkin, J. G. Haasnoot and E. Codjovi, *Inorg. Chem.*, 1994, **33**, 2617–2623;

   b) J.-P. Martin, J. Zarembowitch, A. Bousseksou, A. Dworkin, J. G. Haasnoot and F. Varret, *Inorg. Chem.*, 1994, **33**, 6325–6333;

   c) A. Rotaru, M. M. Dîrtu, C. Enachescu, R. Tanasa, J. Linares, A. Stancu and Y. Garcia, *Polyhedron*, 2009, **28**, 2531–2536.
5. a) P. Ganguli, P. Gütlich and E. W. Müller, *Inorg. Chem.*, 1982, **21**, 3429–3433;

   b) C. Baldé, C. Desplanches, A. Wattiaux, P. Guionneau, P. Gütlich and J.-F. Létard, *Dalton Trans.*, 2008, 2702–2707;

   c) M. S. Sylla, C. Baldé, N. Daro, C. Desplanches, M. Marchivie and G. Chastanet, *Eur. J. Inorg. Chem.*, 2018, 297–304.
6. Z. Yu, T. Kuroda-Sowa, H. Kume, T. Okubo, M. Maekawa and M. Munakata, *Bull. Chem. Soc. Jpn.*, 2009, **82**, 333–337.
7. T. Tayagaki, A. Galet, G. Molnár, M. C. Muñoz, A. Zwick, K. Tanaka, J. A. Real and A Bousseksou, *J. Phys. Chem. B*, 2005, **109**, 14859–14867.
8. J. M. Holland, J. A. McAllister, Z. Lu, C. A. Kilner, M. Thornton-Pett and M. A. Halcrow, *Chem. Commun.*, 2001, 577–578.
9. N. K. Solanki, M. A. Leech, E. J. L. McInnes, F. E. Mabbs, J. A. K. Howard, C. A. Kilner, J. M. Rawson and M. A. Halcrow, *J. Chem. Soc. Dalton Trans.*, 2002, 1295–1301.
10. M. A. Halcrow, *Chem. Commun.*, 2010, **46**, 4761–4763.
11. C. A. Tovee, C. A. Kilner, J. A. Thomas and M. A. Halcrow, *CrystEngComm*, 2009, **11**, 2069–2077.
12. G. M. Sheldrick, *Acta Cryst. Sect. A: Found. Adv.*, 2015, **71**, 3–8.
13. G. M. Sheldrick, *Acta Cryst. Sect. C.: Struct. Chem.*, 2015, **71**, 3–8.
14. L. J. Barbour, *J. Appl. Crystallogr.*, 2020, **53**, 1141–1146.
15. O. V. Dolomanov, L. J. Bourhis, R. J. Gildea, J. A. K. Howard and H. Puschmann*, J. Appl. Crystallogr.*, 2009, **42**, 339–341.
16. J. K. McCusker, A. L. Rheingold and D. N. Hendrickson, *Inorg. Chem.*, 1996, **35**, 2100–2112.
17. P. Guionneau, M. Marchivie, G. Bravic, J.-F. Létard and D. Chasseau, *Top. Curr. Chem.*, 2004, **234**, 97–128.
18. M. A. Halcrow, *Chem. Soc. Rev.,* 2011, **40**, 4119–4142.
19. M. Marchivie, P. Guionneau, J.-F. Létard and D. Chasseau, *Acta Cryst. Sect. B: Struct. Sci.*, *2*005, **61**, 25–28.
20. a) M. A. Halcrow, I. Capel Berdiell, C. M. Pask and R. Kulmaczewski, *Inorg. Chem.*, 2019, **58**, 9811–9821;
    b) E. Michaels, C. M. Pask, I. Capel Berdiell, H. B. Vasili, M. J. Howard, O. Cespedes and M. A. Halcrow, *Cryst. Growth Des.*, 2022, **22**, 6809–6817.
21. L. J. Kershaw Cook, R. Mohammed, G. Sherborne, T. D. Roberts, S. Alvarez and M. A. Halcrow *Coord. Chem. Rev*., 2015, **289–290**, 2–12.

22. a) L. J. Kershaw Cook, F. L. Thorp-Greenwood, T. P. Comyn, O. Cespedes, G. Chastanet and M. A. Halcrow, *Inorg. Chem.*, 2015, **54**, 6319–6330;
b) I. Capel Berdiell, R. Kulmaczewski, N. Shahid, O. Cespedes and M. A. Halcrow, *Chem. Commun.*, 2021, **57**, 6566–6569;
c) N Suryadevara, A Mizuno, L Spieker, S Salamon, S. Sleziona, A. Maas, E. Pollmann, B. Heinrich, M. Schleberger, H. Wende, S. K. Kuppusamy and M. Ruben, *Chem. – Eur. J.*, 2022, **28**, e202103853;
d) R. Kulmaczewski, L. J. Kershaw Cook, C.M. Pask, O. Cespedes and M. A. Halcrow, *Cryst. Growth Des.*, 2022, **22**, 1960–1971.
23. J. M. Holland, C. A. Kilner, M. Thornton-Pett and M. A. Halcrow, *Polyhedron*, 2001, **20**, 2829–2840.
24. R. Pritchard, C. A. Kilner and M. A. Halcrow, *Chem. Commun.*, 2007, 577–579.
25. I. Dance and M. Scudder, *CrystEngComm*, 2009, **11**, 2233–2247.
26. M. J. Cliffe and A. L. Goodwin, *J. Appl. Cryst.*, 2012, **45**, 1321–1329.
27. D. Chernyshov, M. Hostettler, K. W. Törnroos and H.-B. Bürgi, *Angew. Chem. Int. Ed.*, 2003, **42**, 3825–3830.
28. N. Huby, L. Guérin, E. Collet, L. Toupet, J.-C. Ameline, H. Cailleau, T. Roisnel, T. Tayagaki and K. Tanaka, *Phys. Rev. B*, 2004, **69**, 020101(R).
29. J. Kusz, H. Spiering and P. Gütlich, *J. Appl. Cryst.*, 2001, **34**, 229–238.
30. J. Kusz, H. Spiering and P. Gütlich, *J. Appl. Cryst.*, 2000, **33**, 201–205.
31. M. Seredyuk, A. B. Gaspar, J. Kusz, G. Bednarek and P. Gütlich, *J. Appl. Cryst.*, 2007, **40**, 1135–1145.
32. H. E. Mason, J. R. C. Musselle-Sexton, J. A. K. Howard, M. R. Probert and H. A. Sparkes, *New J. Chem.*, 2021, **45**, 14014–14023.
33. J. Kusz, M. Nowak and P. Gütlich, *Eur. J. Inorg. Chem.*, 2013, 832–842.
34. R. Kulmaczewski, E. Trzop, L. J. Kershaw Cook, E. Collet, G. Chastanet and M. A. Halcrow, *Chem. Commun.*, 2017, **53**, 13268–13271.
35. R. Kulmaczewski, E. Trzop, E. Collet, S. Vela and M. A. Halcrow, *J. Mater. Chem. C*, 2020, **8**, 8420–8429.